Article:

Tomassini, L, Parker, DJ, Stirling, A et al. (2017) The interaction between moist diabatic processes and the atmospheric circulation in African Easterly Wave propagation. Quarterly Journal of the Royal Meteorological Society, 143 (709). pp. 3207-3227. ISSN: 0035-9009

https://doi.org/10.1002/qj.3173

The interaction between moist diabatic processes and the atmospheric circulation in African Easterly Wave propagation

Lorenzo Tomassini[a*], Douglas J. Parker[b], Alison Stirling[a], Caroline Bain[a], Catherine Senior[c], and Sean Milton[a]

[a]*Met Office, Exeter, United Kingdom*

[b]*School of Earth and Environment, University of Leeds, Leeds, United Kingdom*

[c]*Met Office Hadley Centre, Exeter, United Kingdom*

*Correspondence to: Met Office, FitzRoy Road, Exeter EX1 3PB, United Kingdom. Email: lorenzo.tomassini@metoffice.gov.uk

An objective tracking algorithm is used to characterise the three-dimensional structure of African Easterly Waves (AEWs) in ERA-Interim reanalysis and a Met Office Unified Model (UM) simulation. A special focus is dedicated to the coupling of dynamical aspects of the wave and moist convection. The relation between baroclinic features of the wave and latent heating is explored. Latent heating at and slightly ahead of the wave trough is found to reinforce and sustain the anomalous wave circulation through potential vorticity (PV) generation and vortex stretching. The coupling of moist processes and the circulation takes place mainly through moisture convergence at lower mid-tropospheric levels, between 850 hPa and 500 hPa. These findings are confirmed and examined in more detail in a case study of a strong AEW based on high-resolution UM simulations. PV tracers are used to investigate how different moist diabatic processes invigorate the wave. Again moisture anomalies are found to be the main contributors to generating small-scale convergence centres and updrafts ahead of the trough at mid-tropospheric levels. Although buoyancy effects are ultimately responsible for the convective uplift, the results suggest that mesoscale circulations associated with the AEW dynamics are crucial in creating the small-scale moist static instabilities and vortices which are essential for the AEW maintenance. Boundary layer mixing and advection from the northern Sahel may create pockets of high-PV air around the trough in some instances, but this mechanism of wave sustainment needs further investigation.

Key Words: African Easterly Waves; Interaction between moist convection and circulation; Convective organisation

Received . . .

1. Introduction

Our understanding of the interaction between moist diabatic processes and the atmospheric circulation is still fragmentary and incomplete. This interaction takes place on a large range of spatial and temporal scales. It is fundamental for weather and climate in the tropics (Charney 1963; Hoskins and Karoly 1981; Hoerling 1992), but plays a crucial role in extratropical weather systems and climate variability as well (Hoskins and Valdes 1990; Parker and Thorpe 1995; Booth *et al.* 2013).

African Easterly Waves (AEWs) are a model case for the interplay between moist diabatic processes and the atmospheric circulation. They grow from finite amplitude disturbances exciting barotropic and baroclinic instabilities at the fringes of the African Easterly Jet (Thorncroft *et al.* 1994a,b; Hall *et al.* 2006). Moist processes are important in sustaining the disturbances as they travel from the Darfur Mountains towards the coast of West Africa (Berry and Thorncroft 2005; Cornforth *et al.* 2009; Berry and Thorncroft 2012).

Various past research efforts have been aimed at investigating wave disturbances over West Africa such as the Global Atmosphere Research Program Atlantic Tropical Experiment (GATE) and the African Monsoon Multidisciplinary Analysis (AMMA) project. Valuable observational data were obtained from these programs which shed light on various features of AEWs (Burpee 1972; Reed *et al.* 1977; Kiladis *et al.* 2006; Barthe *et al.* 2010; Bain *et al.* 2011). New reanalysis data, satellite observations, and high-resolution numerical simulations now allow a more detailed view of the interaction between moist convection, clouds, and boundary layer processes in AEW propagation. In a wider perspective, a better understanding of AEW dynamics can provide insights into the more general nature of the two-way interaction between moist diabatic processes and the atmospheric circulation.

In global weather and climate models the majority of diabatic processes have to be parameterized, and the most persistent and fundamental biases in numerical models are related to those parameterizations. The parameterizations do not operate in isolation, they interact with the atmospheric dynamics and with each other. A better understanding of the interaction between parameterized processes and the atmospheric circulation is thus paramount when it comes to parameterization development. In the present study we investigate the interaction between moist diabatic processes and the atmospheric circulation in AEWs by analyzing observations and reanalysis data as well as simulations with a global numerical model, the Met Office Unified Model. The rationale is that exploring the deficiencies of the model, and conducting sensitivity experiments, will not only guide future model development, but also enhance our understanding of the relevance of specific aspects of the convection-circulation interaction in AEWs.

The aim of the paper is thus to elucidate the role of moist diabatic processes in African Easterly Wave dynamics. The problem may be broken down into three main questions: (1) where does moist convection occur preferentially relative to the wave trough; (2) what is the impact of moist convection on the AEW dynamics at this preferred location; and (3) why does moist convection occur preferentially at this specific location, or in other words, how do AEWs organise convection. These three questions will be addressed and answered in the present study.

The paper has two main parts: a climatological view on the interaction between moist processes and the atmospheric circulation based on objective tracking of AEWs in ERA-Interim and a Unified Model (UM) simulation (Section 2), and a detailed investigation of the case of a strong AEW in July 2010 (Section 3). The first part provides a robust and comprehensive climatological view on the interaction between moist diabatic processes and the AEW dynamics, but the presented composite analysis cannot demonstrate a causal relationship between moist processes and features of the wave development. In the second part a process-based analysis of the diabatic influences on AEW dynamics is then undertaken by means of numerical sensitivity experiments which establish a mechanistic connection between moisture convergence ahead of the wave trough, organised convection, and wave growth. In particular, the paper will use the analysis of diabatic contributions to the potential vorticity (PV) budget of AEWs to quantify the impact of those processes on the synoptic development.

The paper is therefore structured as follows: in Section 2, statistical analysis of AEW diagnostic fields in ERA-Interim will be compared with those fields from a free-running climate version of the Met Office model, to explore the ways in which the differing representation of diabatic processes in the two models is responsible for differing AEW evolution. The discussion is mainly restricted to the southern coastal region of West Africa, but the way dynamical features of the wave structure and related diabatic processes vary across different regions is briefly touched upon. Section 3 proceeds to investigate these processes in more detail through Lagrangian analysis of potential vorticity in a case study with the Met Office model. Finally, in Section 4 the results are summarised and generalised through conceptual exploration of the "diabatic wave" processes.

2. The three-dimensional structure of African Easterly Waves

In this section we use an objective algorithm to track AEWs and to compute wave composites over a climatological period of 11 seasons for the years 1998 to 2008. A season includes the months of July to September when the West African monsoon reaches its most northerly position. The three-dimensional structure of AEWs in ERA-Interim reanalysis and a Met Office Unified Model simulation is discussed, and the relation of the wave disturbances to rainfall and moist diabatic processes analysed.

The AEW composites are computed for six regions separately, i.e. conditional on the wave trough being detected within one of the particular regions. The six regions are denoted North West (NW), South West (SW), North Central (NC), South Central (SC), North East (NE), and South East (SE), and are indicated in Figure 1. Mean fields and the three-dimensional structure of the AEWs will first be discussed in detail for the region South West (SW). Differences that characterize the waves in the NW and SE region will be described separately in Section 2.5.

As pointed out in other studies (e.g., Janiga and Thorncroft 2013), the area of the West African coast is particularly active convectively and the diabatic heating associated with the wave disturbances notedly pronounced. In the eastern regions, over Chad and the Sudan, the AEWs are typically in an early stage of their development and the connection to organised convection potentially weaker. The wave properties in the central areas are a middle ground between the features observed in the west and the east and are not shown for clarity of presentation.

2.1. *Data and methods*

2.1.1. *Data*

For the composite analysis data from the European Centre for Medium-Range Weather Forecast (ECMWF) ERA-Interim reanalysis (Dee *et al.* 2011) are used. Despite the fact that there are rather few atmospheric observations over West Africa, the ERA-Interim reanalysis fields generally show a good agreement with other observational products (Roberts *et al.* 2015). Reanalysis data have been employed in other studies of the climatological structure of African Easterly Waves (Kiladis *et al.* 2006; Berry and Thorncroft 2012; Bain *et al.* 2013; Janiga and Thorncroft 2014; Poan *et al.* 2015).

Rainfall observations from the 3-hourly, 0.25° in latitude and longitude Tropical Rainfall Measuring Mission (TRMM) 3B42 V7 dataset (Huffman *et al.* 2007) for the period 1998 to 2008 are combined with the ERA-Interim data. This precipitation product was evaluated favourably against ground-based observations over West Africa at the temporal and spatial resolution considered here (Guilloteau *et al.* 2016).

A simulation with the Met Office Unified Model in the configuration GA7 at N96 resolution (approximately 150km grid box spacing) using daily varying prescribed sea surface temperatures is analyzed as well.

2.1.2. *African Easterly Wave tracking and composite calculation*

AEWs are tracked based on the objective method described in Bain *et al.* (2013), with some modifications and additions. Here the main features of the algorithm are sketched.

The tracking is based on 6-hourly wind fields at the 700 hPa level. Curvature vorticity is calculated from the wind, and averaged separately over the three latitude bands 5° to 15°, 10° to 20°, and 15° to 25° North. Then the AEWs are tracked for each latitude band. Only AEWs which have a curvature vorticity larger than $c_{min} = 10^{-7}s^{-1}$, at any given time and longitude, are considered.

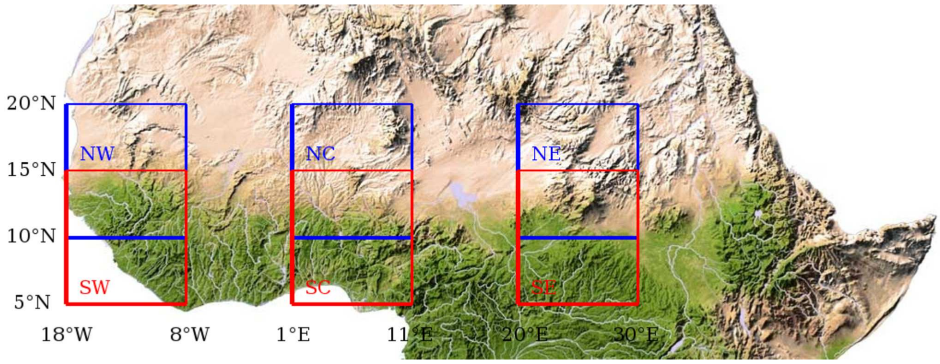

Figure 1. Study region in Africa with the different areas used for the composite analysis.

Based on the tracks on the three latitude bands, a simple criterion is used in order to decide whether waves identified on different latitude bands are manifestations of one single wave. In a last step the location of the wave trough is identified more precisely, starting from the first guess trough longitude determined by the curvature vorticity tracking. This is done in two iterations, based on anomalies of meridional wind and relative vorticity at 700 hPa.

Iteration 1: For every point in time it is first diagnosed on which latitude band the wave is strongest in terms of the median of the curvature vorticity in the vicinity of the first guess trough longitude. Then meridional wind and relative vorticity anomalies are restricted to the identified latitude band. A search is carried out for the longitude lon_{iter1} at which the modulus of the meridional wind anomaly becomes minimal in a neighbourhood around the first guess trough longitude. In the given latitude band, in a window around lon_{iter1}, a search is subsequently performed for the latitude at which the relative vorticity anomaly becomes maximal. This provides the first guess latitude lat_{iter1} of the trough location.

Iteration 2: The steps of the previous iteration are repeated with searches carried out in smaller neighbourhoods of lon_{iter1} and lat_{iter1}. This gives the final values of the trough longitudes and latitudes.

The African Easterly Wave tracking reveals that the AEWs are substantially weaker in the UM simulation compared to ERA-Interim, both in terms of their mean and their maximum curvature vorticity along the tracks (Figure 2). The fact that there are fewer AEWs, and more waves which travel only a short distance, in the model simulation compared to ERA-Interim is related mainly to the minimum curvature vorticity threshold c_{min} in the tracking.

In the computation of the composites for the UM the detected AEWs are resampled such that the number of AEWs considered in the composites for the UM simulation is equal to the number of AEWs in the ERA-Interim composites. As discussed in the Introduction, the rather low-resolution UM simulations analysed in the present section are used to identify and highlight model deficiencies in the representation of convection-circulation interactions and the consequence of these deficiencies for the AEW evolution, not to infer actual properties of the structure of AEWs and related moist diabatic processes. The latter are derived from reanalysis data.

2.2. *Mean state for the South West region*

To understand the structure of the wave anomalies, the climatological conditions in which the waves are embedded have to be considered. Here the mean latitude-height structure of zonal wind, temperature, and specific humidity, averaged over the longitude band used to define the coastal regions, namely 18° to 8° West, is shown for ERA-Interim and the UM (Figure 3).

The mean zonal wind shows the African Easterly Jet (AEJ) with centre at around 600 hPa, and the westerly monsoon flow below (Figure 3, panels a and b). The jet is much less confined in the UM and shifted southward compared to ERA-Interim. The low-level monsoon circulation does not reach as far north in the Unified Model as in ERA-Interim. The temperature structure shows a stronger low-level baroclinicity, i.e. more marked meridional temperature gradients, in the model over the Sahel (Figure 3, panels c and d). Meridional temperature gradients change sign

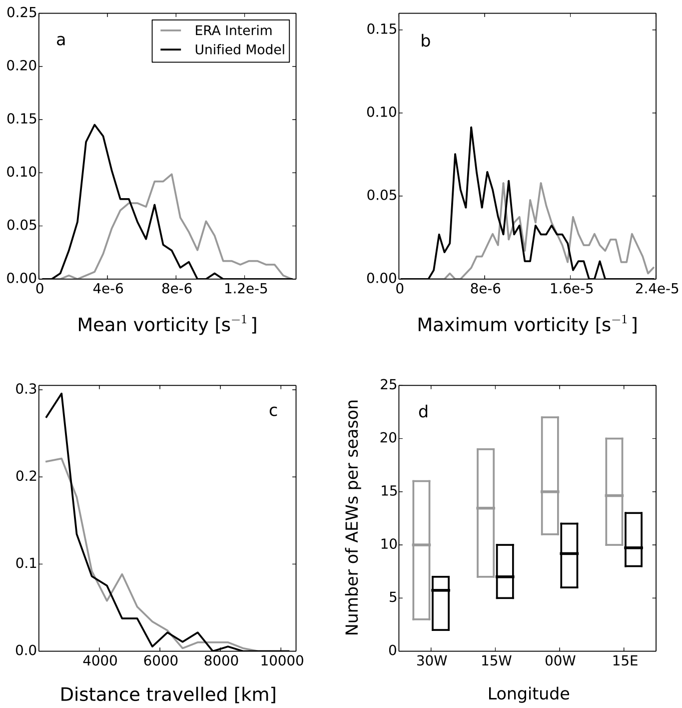

Figure 2. Comparison of African Easterly Waves statistics between Era-Interim and the Unified Model at N96 resolution for the July, August, and September seasons of the years 1998 to 2008: histograms of mean and maximum curvature vorticity along the wave tracks (top row), histograms of the length of the wave tracks, and number of AEWs per season (bottom row), indicating mean, minimum, and maximum values at four different longitudes.

at about the AEJ level, i.e. around 600 hPa. The regions of high humidity reach further north in ERA-Interim (Figure 3, panels e and f). Note that in the southern part of the domain meridional humidity gradients are small in ERA-Interim and become substantial only north of about 15° latitude.

2.3. *Three-dimensional wave structure for the South West region*

Based on the AEW tracking, the composite structure of AEWs is calculated for both ERA-Interim and the UM. Longitude zero in the composites corresponds to the longitude of the wave trough. In this section the discussion is restricted to the South West (SW) region.

2.3.1. *Dynamical fields*

The longitude-height cross sections of the meridional wind anomaly composites reveal that the wave has a more baroclinic structure in the UM than in ERA-Interim at lower levels of the atmosphere (Figure 4, panels a and b). In the UM the wave anomaly slants into the shear whereas in ERA-Interim it shows an upright appearance. This is consistent with the low-level mean meridional temperature gradient being stronger in the UM over the SW region. It also reflects the fact that the AEJ is narrower in ERA-Interim and exhibits stronger meridional gradients in the zonal wind. A stronger meridional gradient in the zonal wind enhances barotropic instability and barotropic energy conversion from the mean flow to the wave disturbance (Thorncroft *et al.* 1994a). Moreover, the signature of the AEJ in the wave composite is more distinct in the UM. This is partly due to the fact that in the model the AEJ is located within the SW region whereas for ERA-Interim it is positioned further north. However, there is evidence that the fact that the anomaly is more concentrated, and broader, at the level of the AEJ in the model is also a result of the nature of the interaction between the convective parameterization and the circulation in the UM (see Sections 2.4 and 3.3).

The characteristics of the meridional wind wave anomaly vary depending on the region because the baroclinicity of the mean state varies. Reed *et al.* (1977) reports a maximum of the meridional wind anomaly at about the AEJ level, a nearly vertical wave axis below 700 hPa, and a westward slope above, in agreement with our results for the SW. Burpee (1972), who considers a more northern region, describes a distinct tilt a

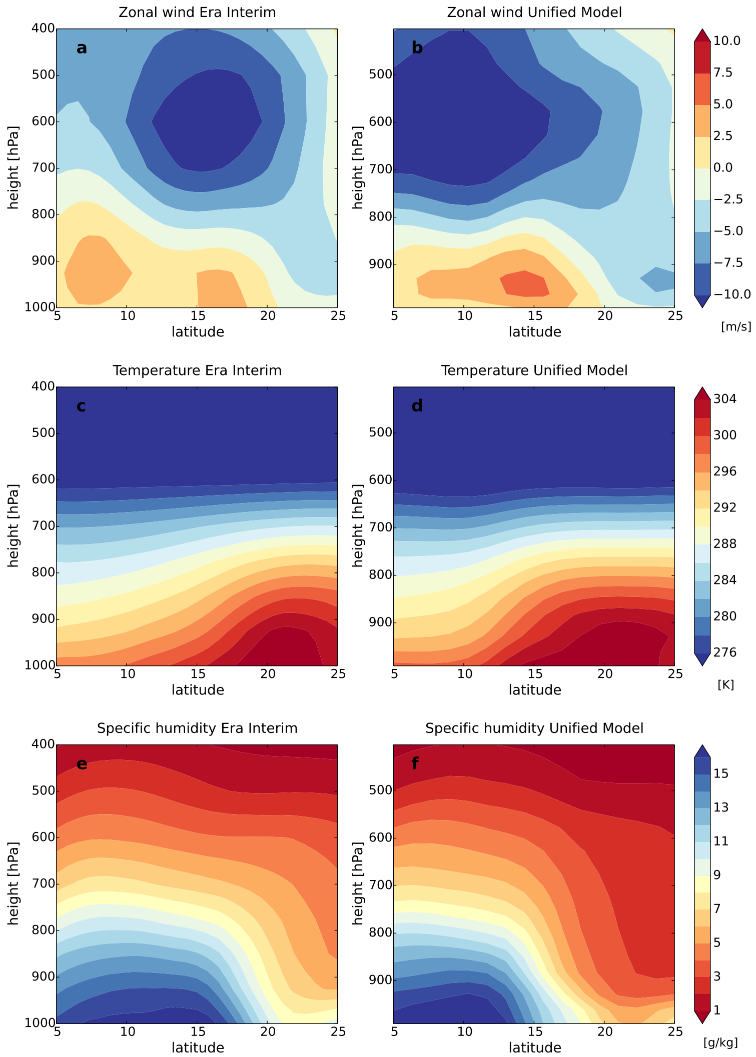

Figure 3. Mean cross sections of zonal wind (top row), temperature (middle row), and specific humidity (bottom row) averaged over the longitudes of the coastal regions over the years 1998 to 2008, for Era-Interim (left column) and the Unified Model (right column).

low levels. Consistently, Reed *et al.* (1977) notes that baroclinic instability contributes more to wave growth in northern areas, whereas further south baroclinicity is weaker and precipitation heavier. Also the vertical structure of latent heating plays a role in defining the structure of the wave disturbance. Idealized studies suggest that low-level latent heating supports barotropic energy conversion and a more barotropic appearance of the wave, whereas a top-heavy heating profile favours baroclinic wave growth (Padro 1973; Craig and Cho 1988; Thorncroft *et al.* 1994b; Hsieh and Cook 2007).

The horizontal structure of the meridional wind in ERA-Interim suggests that in the along-trough direction geostrophic balance is a good approximation (not shown). This makes the semi-geostrophic conceptual framework of Parker and Thorpe (1995) attractive for the interpretation of the AEW dynamics (see Section 4).

Composites of potential vorticity anomalies indicate a deeper and narrower anomaly in ERA-Interim compared to the model (Figure 4, panels c and d). As with the meridional wind, the anomaly is located in a wider region around the trough in the model, whereas in ERA-Interim it is positioned at or slightly ahead of the trough. At around 800 hPa the PV anomalies extend to regions behind the trough in both ERA-Interim and the UM, a circumstance which is due to enhanced stability associated with low-level cold advection in that area.

Zonal wind anomaly composites in ERA-Interim show the slowdown of the easterly wind at the level of the AEJ (Figure 4, panels e and f for ERA-Interim). The low-level monsoon flow is strengthened somewhat ahead of the trough. Viewing the wave trough as a frontal system conceptually, as suggested in Bain *et al.* (2011), an easterly ageostrophic low-level cross-frontal circulation is identifiable which has its centre in the

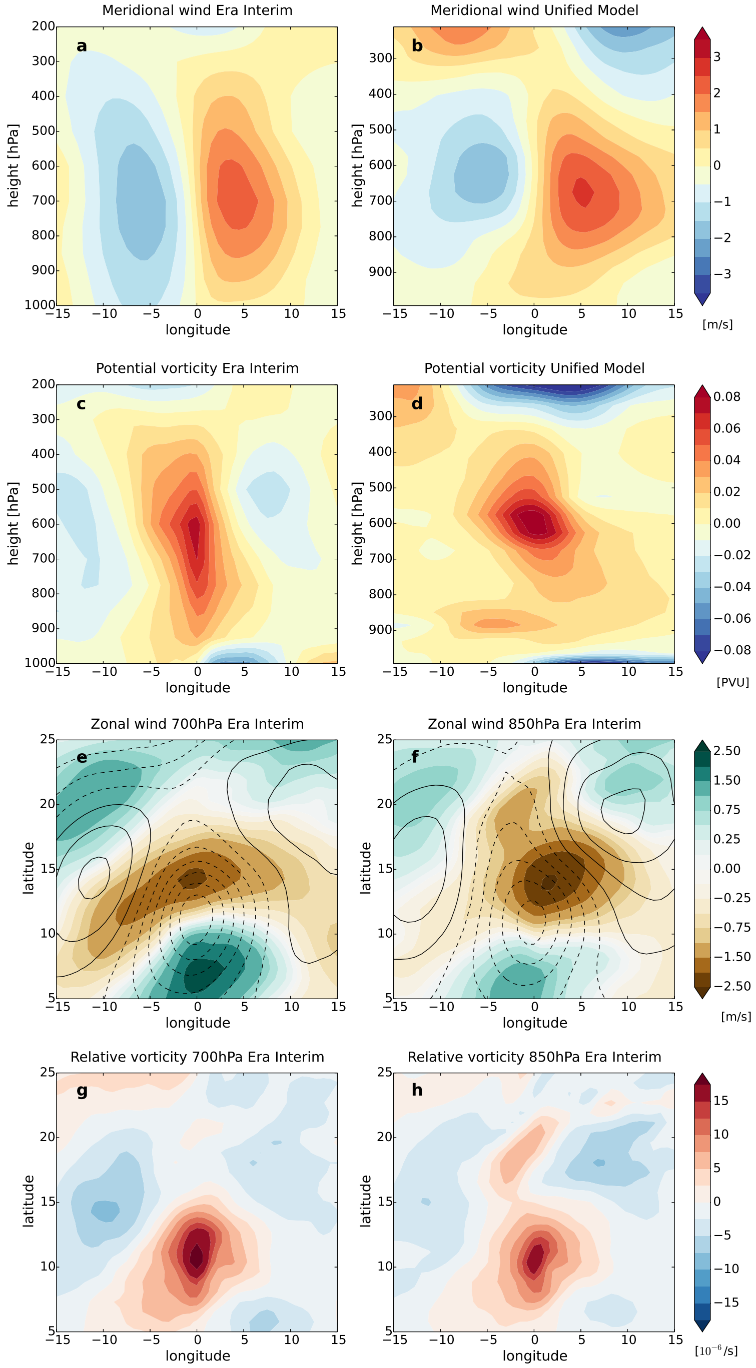

Figure 4. Composites of meridional wind (panels a and b) and PV (panels c and d) anomalies conditional on the African Easterly Wave being detected in the region SW, for Era-Interim and the Unified Model. Panels e and f show composites of zonal wind anomalies at 700 hPa and 850 hPa for ERA-Interim, respectively. Black contours indicate geopotential height anomalies (contour lines are ±6, ±5, ±4, ±3, ±2, ±1, and 0 m). Bottom row: composites of relative vorticity anomalies at 700 hPa (panel g) and 850 hPa (panel h) for ERA-Interim. The zero longitude corresponds to the trough location of the wave.

northern part of the wave slightly ahead of the front at 700 hPa, and slightly behind the front at 850 hPa (Figure 4, panels e and f; the black contour lines indicate geopotential height anomalies). At around the AEJ, regions of westerlies correspond to regions of southerlies, and regions of easterlies correspond to regions of northerlies, indicating that the wave transports easterly momentum northward. This suggests barotropic energy conversion from zonal kinetic energy to eddy kinetic energy at around the level of the AEJ, in agreement with Reed *et al.* (1977).

At 700 hPa the relative vorticity anomaly pattern tilts slightly from southwest to northeast, but not very markedly so (Figure 4, panel g for ERA-Interim). At the 850 hPa level there is a second vorticity centre to the north slightly ahead of the main wave, a feature also described by Reed *et al.* (1977) and Berry and Thorncroft (2005) (Figure 4, panel h for ERA-Interim). This second vorticity centre is more pronounced in other regions (not shown).

2.3.2. *Temperature and humidity*

Comparing temperature anomalies between ERA-Interim and the UM (Figure 5, panels a and b) confirms the more baroclinic structure of the wave disturbance in the model due to the stronger mean temperature gradients over the region. There are other important differences. In the model the southerly advection of cold air is much stronger, and the wave has a cold core below the level of the AEJ behind as well as in front of the trough. In ERA-Interim there are indications of a warm and a cold conveyor belt in the lower troposphere. Warm and dry air is drawn in from the north, cold air is advected from the south behind the trough at around 850 hPa (Figure 5, black contour lines in panel f for ERA-Interim). At 700 hPa the cold anomaly corresponds to northerly winds, suggesting that cold air is partly lifted to middle tropospheric levels in a conveyor belt circulation (Figure 5, black contour lines in panel e for ERA-Interim). The anomaly patterns in ERA-Interim agree well with what Reed *et al.* (1977) found in observations. The temperature anomalies are also a result of the interaction between baroclinic growth and diabatic heating from convection. Over the SW region, in the model the latent heat release takes place mainly at the upper levels of the troposphere, whereas in ERA-Interim the latent heating is bottom-heavy and occurs throughout the free troposphere (see Section 2.4). The broad warm anomaly in the upper troposphere around the trough in the model is thus partly a consequence of latent heat release induced by the convection parameterization, as shown by the temperature tendency anomaly from the convection parameterization (Figure 6, panel g).

The height-longitude moisture anomaly composites show the anomalous moisture at and slightly ahead of the trough (Figure 5, panels c and d). In ERA-Interim there is a dry anomaly behind the trough because moisture is transported out of this region towards the area at and in front of the trough where it feeds convective development. The horizontal specific humidity anomalies at 850 hPa and 700 hPa correspond well to the temperature anomalies (Figure 5, panels e and f). In the UM a dry anomaly cuts through the trough at low levels. The wide dry region at low levels around the trough in the UM is mostly caused by convective drying by the convection parameterization, as demonstrated by the composite of the convective specific humidity tendency (Figure 6, panel h).

2.4. *Relation to precipitation and moist diabatic processes*

Precipitation formation is intimately linked to latent heat release in the atmosphere. A comparison of the location of TRMM precipitation relative to the ERA-Interim wave trough and the UM precipitation and respective wave trough is shown in Figure 6, panels a and b. This reveals that precipitation is formed in a rather narrow band ahead of the trough in ERA-Interim, whereas for the UM precipitation is distributed in a broader region around the trough and confined to more southern areas. In the model there is a northern extension of the precipitation anomaly behind the trough related to strong positive moisture anomalies.

The anomaly composite for vertical pressure velocity is consistent with the precipitation characteristics in terms of the spatial position (Figure 6, panels c and d). It also shows a strong maximum at upper levels in case of the model whereas for ERA-Interim strongest upward velocities occur at lower levels ahead of the trough. In extra-tropical baroclinic waves latent heating most strongly couples with the dynamics at low levels where temperature and moisture advection is strongest. As discussed in more detail below, in the AEW case convection and dynamics are coupled most strongly through pre-frontal moisture convergence and diabatic PV generation at lower mid-tropospheric levels, i.e. between 850 to 500 hPa (Figure 4, panel c, and Figure 5, panel c; see also Berry and Thorncroft (2012) and the discussion in Section 3.4).

A robust diagnostic of latent heating which can also be calculated for the ERA-Interim reanalysis is the so-called apparent heat source (Yanai *et al.* 1973). Let T denote temperature, z geopotential height, g the gravitational constant, and c_p specific heat at constant pressure. From the budget equation for dry static energy $s = c_pT + gz$ it follows that approximately

$$\frac{\partial T}{\partial t} + \nabla \cdot (\mathbf{V}T) = Q^{\mathrm{Rad}} + Q^{\mathrm{Latent}} - \frac{\partial}{\partial p}(\omega' T') \qquad (1)$$

where $\mathbf{V}$ denotes the three-dimensional wind vector, Q^{Rad} diabatic heating from radiation, Q^{Latent} latent heating, and $(\omega' T')$ subgrid-scale turbulent heat fluxes in pressure coordinates.

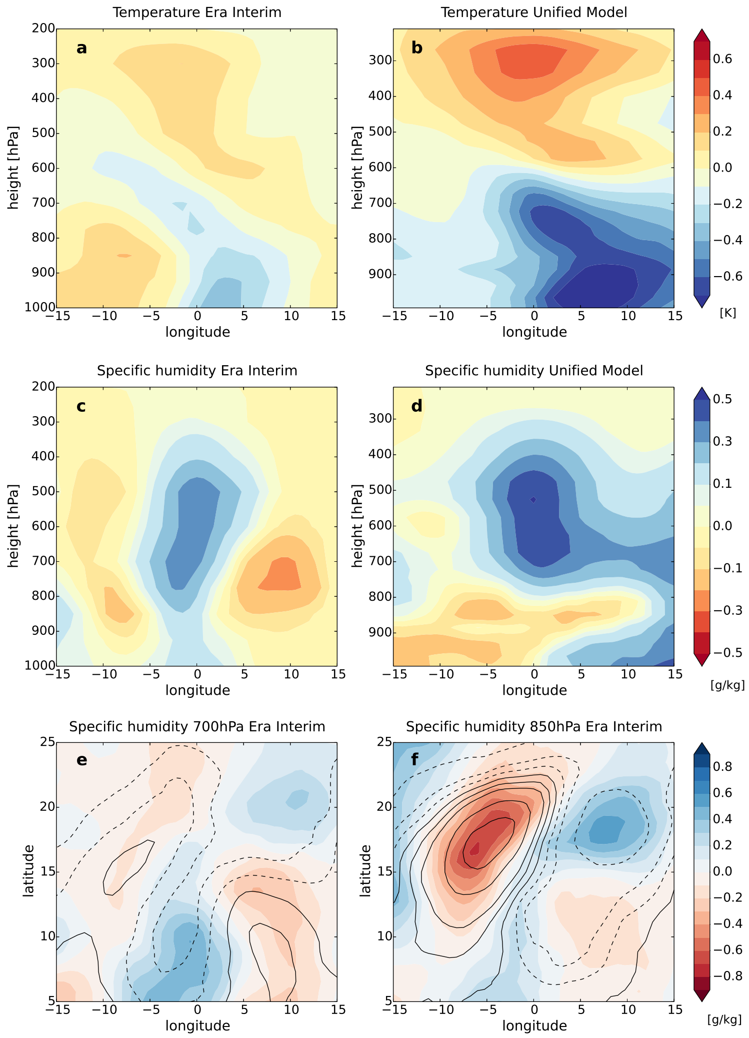

Figure 5. Composites of temperature (top row) and specific humidity anomalies (second row) conditional on the African Easterly Wave being detected in the region SW, for Era Interim (panels a and c) and the Unified Model (panels b and d). Panels e and f: composites of specific humidity anomalies for ERA-Interim at 700 hPa and 850 hPa, respectively. Black contours indicates corresponding composites of temperature anomalies (contour lines are ± 1, ± 0.8, ± 0.6, ± 0.4, ± 0.2, ± 0.1, and 0 K). The zero longitude corresponds to the trough location of the wave.

Defining

$$Q_1^R := \frac{\partial T}{\partial t} + \nabla \cdot (\mathbf{V}T) - Q^{\mathrm{Rad}} \qquad (2)$$

thus provides an approximate expression for the sum of the latent heating Q^{Latent} plus the subgrid-scale turbulent heat flux convergence term using rather robust large-scale quantities, which are constrained by observations in ERA-Interim.

Indeed, wave composites of Q_1^R anomalies agree well with composites of convective heating tendency anomalies in the model (compare Figure 6, panel f, with panel g). For the South West region the Q_1^R anomaly composites are shown in Figure 6, panels e and f. The UM Q_1^R composite shows a top-heavy deep convective profile which is not very well aligned with the trough. In ERA-Interim the anomaly in the vertical gradient of Q_1^R exhibits a maximum at around 700 hPa suggesting strongest diabatic PV generation at around this height. This is in agreement with results by Janiga and Thorncroft (2013) who also find maximum latent heat release in the lower mid troposphere at the coast of West Africa, and top heavy heating profiles in eastern regions, consistent with the analysis presented in Section 2.5.

Why does precipitation, and thus organised convection, occur preferentially at and slightly ahead of the trough? Anomaly composites of moist static energy (MSE) at 925 hPa show that in the model there is a negative anomaly around the trough in the region where precipitation forms (Figure 7, panel b). This is partly a result of convective drying (Figure 6, panel h). But also in ERA-Interim the low-level MSE anomaly is small in the area at and slightly ahead of the trough (Figure 7, panel a). This suggests that in AEWs convection is not primarily controlled by boundary layer moist static stability anomalies. Rather, convective activity is governed mainly by

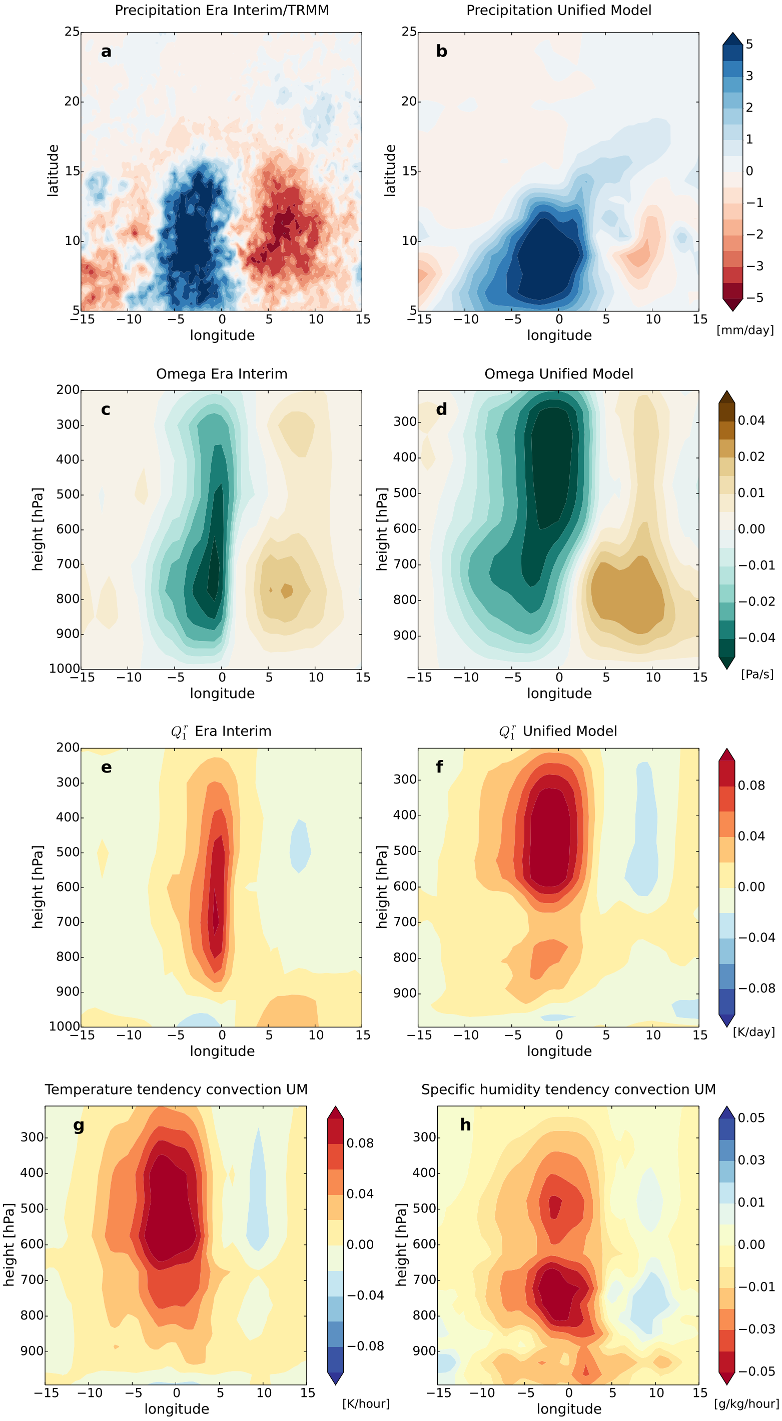

Figure 6. Composites of precipitation (top row), vertical pressure velocity (second row), and Q_1^r (third row) anomalies conditional on the African Eastery Wave being detected in the region SW, for Era Interim (left column) and the Unified Model (right column). For the precipitation anomaly composite in panel a, TRMM rainfall data is used. Panels g and h: composites of convective temperature and humidity tendency anomalies, respectively, for the UM. The zero longitude corresponds to the trough location of the wave.

moisture convergence at lower mid-tropospheric levels (Figure 7, panels c and d, for the 850 hPa level). In ERA-Interim there is a distinct convergence line ahead of the trough where precipitation is located. The area at and slightly ahead of the trough is the region of preferred moisture convergence in the anomalous wave circulation as discussed in more detail for the case presented in Section 3 (see also the conceptual summary in Section 4). Of course moisture convergence can partly be a result of convection. But the evidence suggests that lower mid-tropospheric moisture convergence generated by the wave dynamics is key in triggering and organising convective cells.

The convection parameterization in the UM shows too little sensitivity to the resolved dynamics of the wave and moisture anomalies in the middle troposphere. Also the fact that at 150 km grid spacing the model is not able to resolve the mesoscale dynamics of the wave, and circulations related to organised convection, sufficiently well contributes to the deficient representation of the convection-circulation interaction in the UM.

2.5. *Differences among regions*

In this paragraph we briefly summarise the climatological view on the convection-circulation interaction in AEWs for two other regions, the North West and the South East (Figure 1). The mean state of the atmosphere varies across regions, such as meridional temperature, humidity, and zonal wind gradients, and the position of the AEJ. These aspects impact the structure of the waves and the relative importance of different energy conversion processes. An indirect effect of the mean state of the atmosphere, together with orographic features, is the differing importance and characteristics of mesoscale convective systems (MCSs) and related latent heat release. For instance, in the northern part precipitation is scarcer due to the drier environment, and organized convective systems related to the AEWs are embedded in more stable upper-tropospheric environments (Houze 1989, 2004). This has in turn an impact on the AEW structure.

Mean cross sections for the eastern longitudes (not shown) show that the AEJ is positioned further south compared to the coastal region, and is weaker. The monsoon, as indicated by the low-level moisture and temperature gradients and the low-level westerlies, reaches less far north in the central and eastern areas compared to the West Coast, only to about 16° North. Low-level temperature gradients over the SE region are however similar to the gradients over the SW because the southern part of the area is warmer and drier in the SE due to the absence of the sea to the south. Strongest humidity gradients are located at around 15° North.

The height-longitude meridional wind anomaly composite for ERA-Interim reveals that the waves are more baroclinic in the NW compared to the SW because meridional temperature gradients are much stronger in the northern coastal area (Figure 8, panel a). This is also evident in the temperature and specific humidity anomalies (not shown), which are strongest in the more northern parts of the waves. The area starting from about 2 to 3 degrees longitude in front of the trough is dominated by the southward advection of warm and very dry air from the north. Accordingly, the precipitation composite slants somewhat from southwest to northeast (Figure 8, panel c). The vertical pressure velocity shows a very distinct maximum at low levels, below the AEJ (Figure 8, panel e), reflecting the stable environment at upper levels. This is a feature of the waves over all the northern regions NW, NC, and NE. Diabatic processes also peak at low levels (Figure 8, panel g). The strong low-level centre of vertical motion is thus likely a combination of strong low-level baroclinic energy conversion together with latent heating from relatively shallow MCSs, which are capped by a stable upper troposphere (Houze 1989). Generally energy supply by latent heat release is overall weaker in the drier northern region than further south where moisture is more abundant.

In the SE (see Figure 1) the AEJ is located further south compared to the coastal region, meaning that the AEJ is positioned over the area. But the AEJ is considerably weaker here, many of the AEWs are initiated around the Darfur Mountains. Meridional temperature and moisture gradients are weak from 5° North to about 13° North because there is no sea to the south as on the West Coast.

In accordance with the AEJ being weaker, the wave anomalies in the meridional wind are smaller (Figure 8, panel b). Also, since the AEJ is located over the region, there is a stronger imprint of the AEJ in the composite compared to the SW region, and the anomalies are contained mainly to the middle troposphere. There is rather little baroclinic structure at low levels, in stark contrast to the NE region where the positive meridional wind anomaly is confined to levels below the AEJ, and shows strong baroclinic characteristics (not shown).

Temperature and specific humidity anomalies in the SE look rather similar to the corresponding anomalies in the SW (not shown). The negative temperature anomaly is somewhat stronger around the trough in the SE because the positive temperature anomaly due to warm advection from the north does not penetrate as far south as in the SW.

There seems to be a certain contradiction between the precipitation composite and the vertical pressure velocity composite in the SE region (Figure 8, panels d and f). The rainfall composite appears to indicate that there is a rather loose association between precipitation formation and the AEW trough. Both the vertical pressure velocity as well as the Q_1^R anomaly

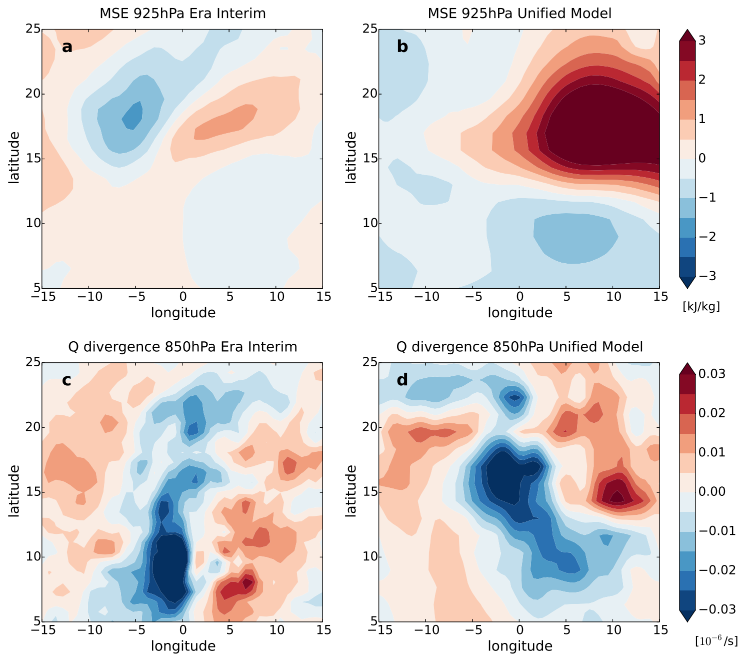

Figure 7. Moist static energy (MSE) anomaly composite at 925 hPa for ERA-Interim (panel a) and the Unified Model (panel b). Moisture divergence anomaly composite at 850 hPa for ERA-Interim (panel c) and the Unified Model (panel d). The zero longitude corresponds to the trough location of the wave.

composite (Figure 8, panel h) suggest otherwise, and show a deep-convective profile. Janiga and Thorncroft (2013) also report top-heavy latent heating profiles in eastern parts of the study region, in contrast to more bottom-heavy profiles at the West Coast and over the Atlantic ocean. In most part of the SE region moisture availability and mean rainfall is high. Since the AEW are typically rather weak dynamically in the area, and moreover are in a developing phase, we conjecture that the ERA-Interim reanalysis struggles to place the AEWs at the exact right location. This is also confirmed in the AEW case study presented below in Section 3. Therefore the composite produced using the TRMM rainfall observation data appears to some degree inconsistent with the passage of the wave. The rainfall composite computed with precipitation from the ERA-Interim reanalysis itself shows a strong signal and is quite well aligned with the trough (not shown), in accordance with the vertical wind and Q_1^R composite. The weak rainfall signal derived based on the TRMM rainfall data might therefore partly be due to the fact that the exact timing and location of the AEW developments are somewhat inaccurately captured in ERA-Interim due to the limited availability of observations in the region. But as suggested by Fink and Reiner (2003) and Janiga and Thorncroft (2016), the connection between AEWs and MCSs is likely weaker over the Soudanian region compared to the coast of West Africa.

The orography in eastern regions might play a certain role in decoupling the rainfall from the AEW trough, and the AEWs tend to be in a developing phase, and weaker in the East compared to the West Coast, and therefore less likely to force MCSs (Fink and Reiner 2003). However, we did not find evidence for a systematic relative position of MCSs behind the trough in eastern parts of North Africa.

3. Case study of a strong African Easterly Wave

From the climatological analysis in the previous section a tentative picture of the convection-circulation interaction in AEWs emerges, which hints at an important role of moisture convergence and convective development at and slightly ahead of the trough. But the statistical perspective does not allow for demonstrating a causal relationship between the AEW dynamics and moist diabatic processes. A case study is therefore used to investigate the two-way interaction between diabatic processes and the atmospheric circulation in AEW propagation in greater detail and with a process-based focus.

3.1. Case study description

In the following a wave disturbance is studied which is clearly detectable starting from 18:00 UTC on July 7, 2010, over North Africa. In order to investigate the case in detail, simulations with

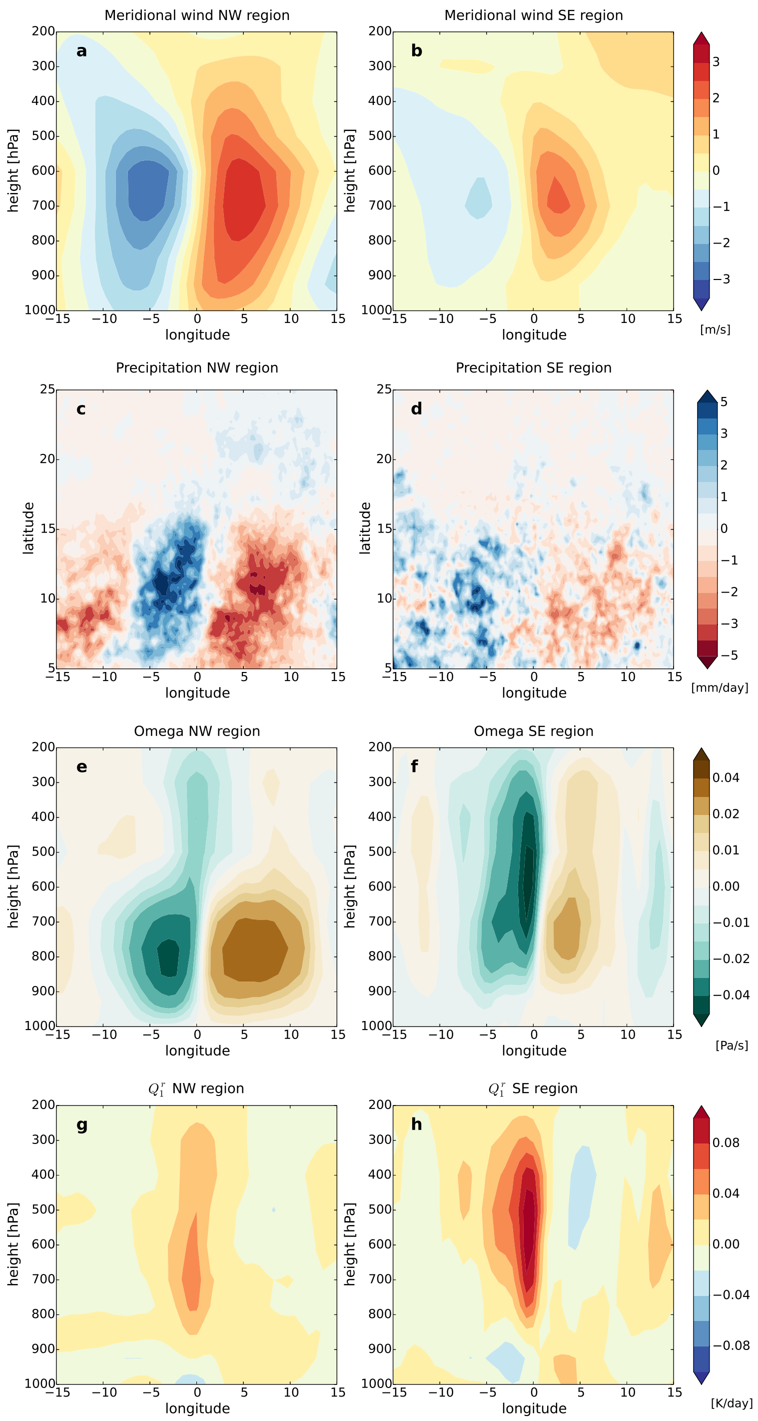

Figure 8. Composites of meridional wind (top row), precipitation (second row), vertical pressure velocity (third row), and Q_1^r (bottom row) anomalies for the NW region (left column) and the SE region (right column). The composites are based on Era-Interim reanalysis. In the precipitation composites (panels c and d) TRMM rainfall data is used. The zero longitude corresponds to the trough location of the wave.

the UM in the global configuration GA7 were performed at N1280 resolution, corresponding to a grid size of about 10 km in the midlatitudes. Forecasts were initialised with ECMWF analysis at six start times: 00:00 UTC on July 7, 18:00 UTC on July 8, 00:00 UTC on July 10, 00:00 UTC on July 11, 18:00 UTC on July 12, and 00:00 UTC on July 14. To minimize issues related to the inability to correctly simulate the diurnal cycle of convection by the convection parameterization, only the mid-level convection scheme is enabled in all of the subsequent hindcast simulations. Mid-level convection treats convective cells which have their root not in the boundary layer but originate at levels above the boundary layer, which is the predominant type of convection encountered in organised convection related to AEWs.

3.2. *Development of the wave*

Figure 9 shows outgoing longwave radiation from 1 $\times$ 1 degree resolution CERES satellite observations (left column) and the model reference simulation at different stages of the wave. The black vertical line indicates the position of the wave trough as diagnosed from the meridional wind of the ECMWF operational analysis. For the first three snapshots the model is initialized at 00:00 UTC on July 7, for the scene on July 11 the model is initialized at 00:00 UTC on July 10, and for the last scene the model is initialized at 00:00 UTC on July 11. Figure 10 shows corresponding precipitation from TRMM (left column) and the reference model simulation (right column) at the same times and using the same forecast initial times as in Figure 9. Figure 11 contains Hovmuller plots of meridional wind and potential vorticity from the operational analysis and the model, and rainfall from TRMM and the model. For the Hovmuller plots of meridional wind, potential vorticity, and precipitation, the data was averaged between 10° to 20° North.

The dynamics of the wave is rather weak over the first 30 hours after detection, i.e. until about 00:00 UTC on July 9 (Figure 11, panels a and c). CERES images show large cloud clusters around the trough, and TRMM exhibits organized precipitation from MCSs in the vicinity of the trough starting from late afternoon on July 8 (Figure 11, panel e). Although the model produces cloud clusters in the region, they are not clearly associated with the dynamics of the wave, and there is hardly any precipitation at or ahead of the trough (Figure 11, panel f). In fact, at this stage the model mainly produces precipitation at around 12:00 UTC, and precipitating cloud clusters unrealistically propagate eastwards probably due to convectively generated gravity waves (Figure 11, panel f).

Note that the wave trough location is slightly different in the analysis compared to the model although the UM is initialized from the analysis (solid and dotted red lines in Figure 11, panels b, d, and f). This confirms the supposition expressed in Section 2.5 that there can be uncertainty about the exact position of the wave trough in the early stage of the wave development.

Starting about July 9 03:00 UTC a crucial strengthening phase of the wave occurs, which lasts for about 2 days (indicated by the yellow shading in the Hovmuller plots). TRMM now shows distinct organized precipitation ahead of the trough at around 12 to 18 degrees North where the main centre of the wave disturbance is located (Figure 10). This is consistent with CERES scenes, which exhibit signatures of corresponding MCSs (Figures 9). This association between precipitation and the wave trough is completely absent in the model at this stage, even at forecast lead times of about 24 hours, a common problem in models with parameterised convection (Skinner and Diffenbaugh 2013). In the model, convection is not sufficiently supported overnight. Likely this is key to the existence of organised systems in the region at and ahead of the trough. Crucially, the wave does not strengthen dynamically over the period of July 9 and July 10 in the UM (Figure 11, panels b and d). This demonstrates the pivotal role of moist convection and associated latent heating in invigorating and sustaining the wave.

There is a second strengthening phase, starting at about July 12 18:00 UTC, when again TRMM shows large MCSs ahead of the wave trough (Figure 11, panel e). At this stage the wave disturbance is already strong and the model, when initialized correctly, manages not only to simulate the wave disturbance, but also to develop associated rainfall and reproduce the involved strengthening of the dynamics (Figure 11, panels b, d, and f). However, this only happens when the wave is vigorous enough to force convective precipitation at the right time and location (Figure 11, panel f). Note that the erroneous diurnal cycle signal as well as the eastward propagating systems are now absent in the reference simulation of the UM in this phase, and the rainfall is dominated by the propagating wave. This stage also coincides with the wave reaching the Guinea Highlands. Here, with the strong orographic forcing and moisture fluxes from the ocean, the model is more likely to sustain convection overnight.

3.3. *The interaction between circulation and latent heating*

The reference simulation with the UM does not reproduce the first crucial strengthening phase of the wave because of the absent interaction of the circulation with moist convection. In the UM convection is represented by a mass flux parameterization based originally on Gregory and Rowntree (1990), with further developments. In the GA7 configuration used here the convective

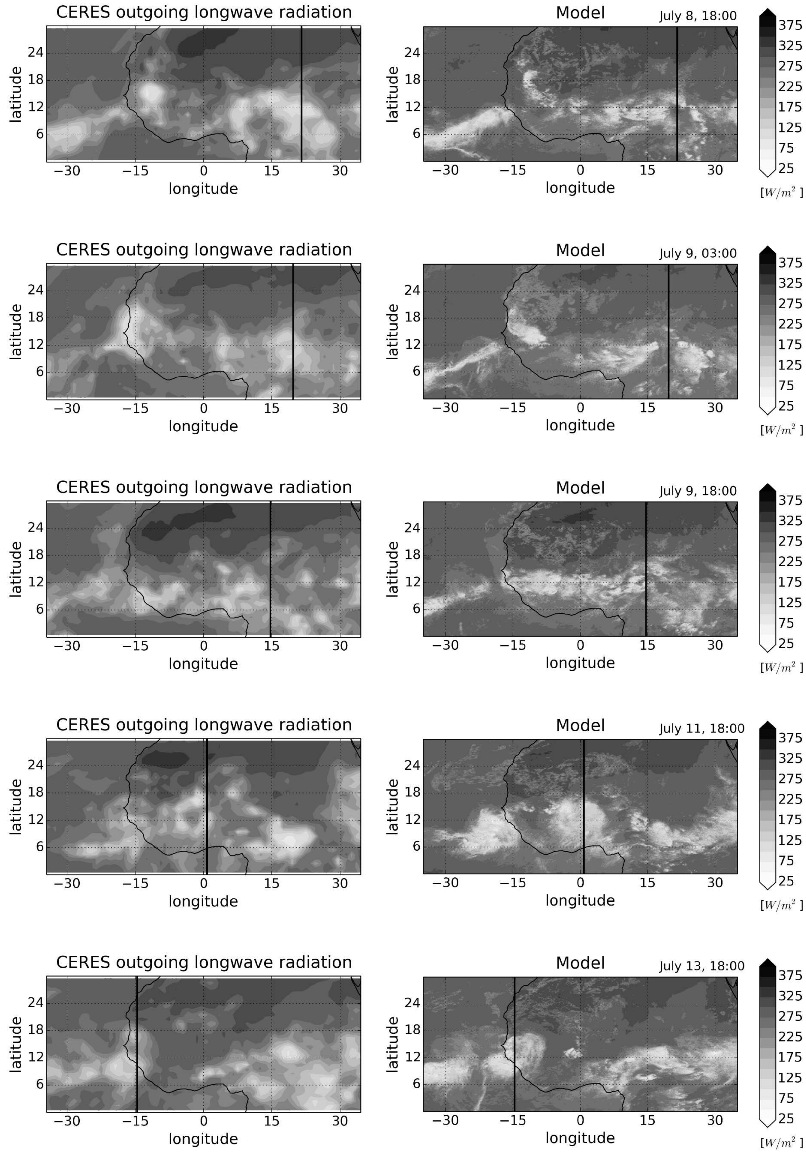

Figure 9. Outgoing longwave radiation from the Clouds and the Earth's Radiant Energy System (CERES) $1^\circ \times 1^\circ$ satellite product (left column) and the UM N1280 (10km) simulation (right column) at five different times. The model is initialized on July 7 at 00:00 UTC, on July 10 at 00:00 UTC, and on July 11 at 00:00 UTC from ECMWF analysis. Vertical black lines indicate the wave trough location as derived from ECMWF analysis.

available potential energy (CAPE) closure includes a dependency of the CAPE timescale on the grid-mean vertical velocity, but generally the CAPE timescale is around half an hour.

In the following results from a sensitivity experiment, denoted "long CAPE timescale" simulation, are described in which the CAPE timescale is fixed and increased to 3 hours. This reduces the parameterised convective mass-flux and the parameterised consumption of CAPE in the model, so that convection can be sustained longer, with weaker intensity. Figure 12 shows Hovmuller plots of potential vorticity at 700 hPa and rainfall for the reference simulation (panels a and c) and the long CAPE timescale simulation (panels b and d). In order to bring out more clearly the fact that the reference simulation is not able to sustain the wave properly, only two forecast initial times are used for the subsequent Hovmuller plots: July 7 00:00 UTC and July 11 00:00 UTC. The lack of precipitation along the wave track, and the failure to intensify the wave through moist diabatic processes, is clearly evident in the reference simulation. In stark contrast, the long CAPE timescale simulation exhibits strong MCSs ahead of the trough, and the wave intensifies over the course of July 9 and 10. The precipitation along the wave track is somewhat overestimated in the long CAPE timescale simulation, and the potential vorticity Hovmuller plot suggest that the wave is slightly too fast (Figure 12, panel b). This indicates that latent heat release ahead of the trough may increase the wave speed, consistent

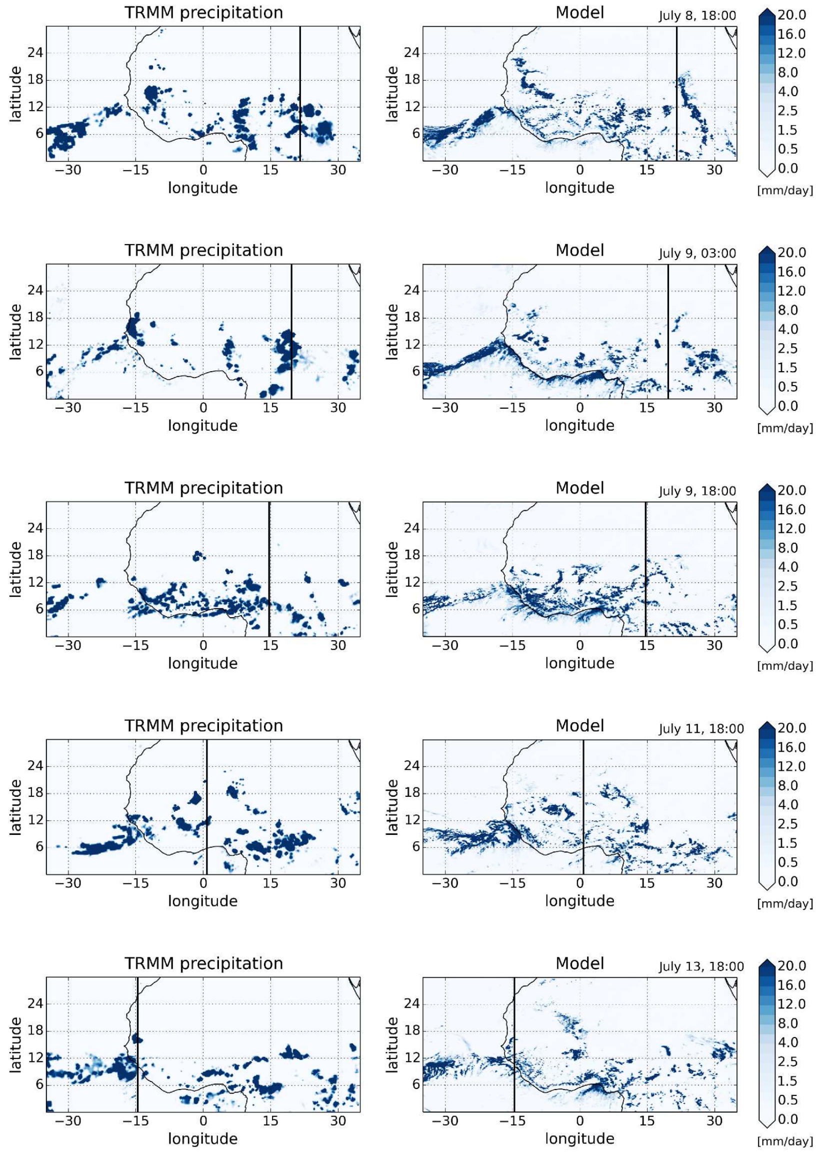

Figure 10. TRMM (left column) and UM N1280 (10km) simulated precipitation (right column) on the days and times shown in Figure 9. Vertical black lines indicate the wave trough location as derived from ECMWF analysis.

with the fact that the wave travels faster in the later stage when associated rainfall becomes intense.

Other sensitivity experiments have been carried out, including a simulation with the convection parameterization turned off completely. However, omitting the convection parameterization entirely leads to unrealistic stationary precipitation features. A certain limited amount of parameterized subgrid convective mass flux is beneficial. Nevertheless, the main difference between the reference simulation and the long CAPE timescale simulation is that in the reference simulation precipitation is handled almost exclusively by the convection parameterization, whereas in the long CAPE timescale simulation rainfall is mainly generated by the large-scale precipitation scheme (not shown). The large-scale precipitation scheme responds directly to the resolved dynamics, unlike the convection parameterisation which does not ”feel” convergence directly.

Figure 13 shows cross sections of the mean temperature tendency of the convection parameterization (panels a and b) and the temperature tendency of the sum of the convection parameterization and the large-scale precipitation scheme (panels c and d) along the wave track for both the reference simulation and the long CAPE timescale simulation. Mean PV is overlaid as black contours. Longitude zero corresponds to the location of the wave trough. For PV, qualitatively the finding is very similar to the results presented in Section 2.3. The PV signature in the long CAPE timescale simulation is deeper, narrower, and more

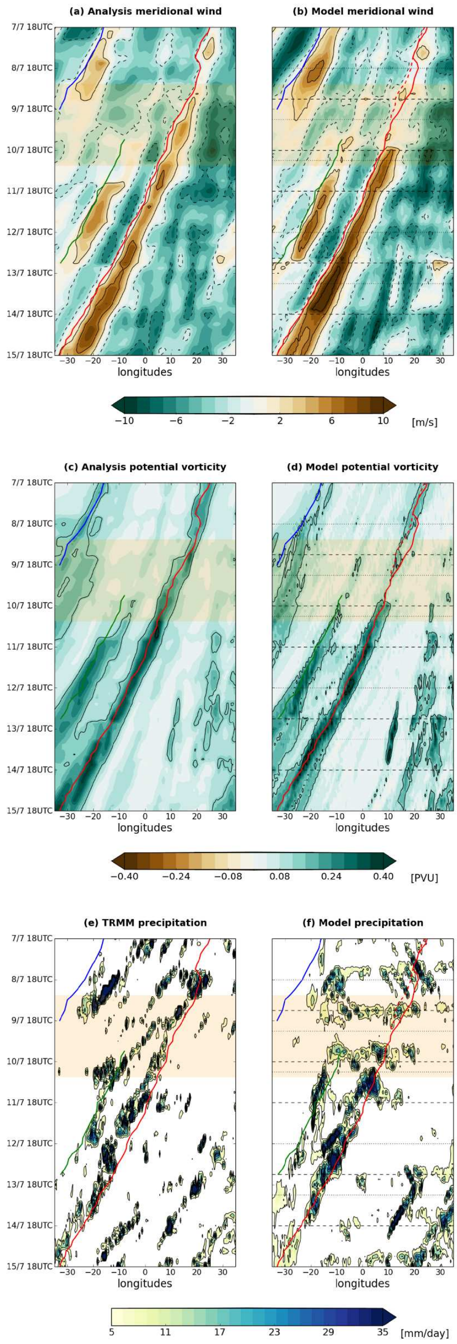

Figure 11. Hovmuller plots of meridional wind (top row), potential vorticity (middle row), and precipitation (bottom row) based on the ECMWF operational analysis (panels a and c), TRMM rainfall data (panel e), and the UM N1280 (10km) reference simulation (panels b, d, and f). The red solid line indicates the wave trough track as diagnosed from the analysis, the red dotted line as determined from the UM simulation. Blue and green lines indicate other waves which are not considered here. All forecast initial times are used for the UM (see Section 3.1). Horizontal dotted lines indicate forecast initialisation times, horizontal dashed lines indicate from which time on the data of a new forecast are used.

strongly confined to the area at and slightly ahead of the trough. In the reference simulation the PV signature is weaker, broader, and more restricted to the level of the AEJ. The temperature tendency of the convection parameterization in the reference simulation does not well align with the trough. In the long CAPE timescale simulation most of the latent heating comes from the large-scale precipitation scheme, which is more intimately coupled to the resolved circulation. It occurs slightly ahead of the trough where strongest updrafts develop. This suggests that the top-heavy heating profile of the deep convection parameterization discussed in Section 2 is not per se problematic. The main issue is the fact that the convection parameterization does not activate at the right time and location relative to the dynamics of the wave, as already hypothesized in Section 2.

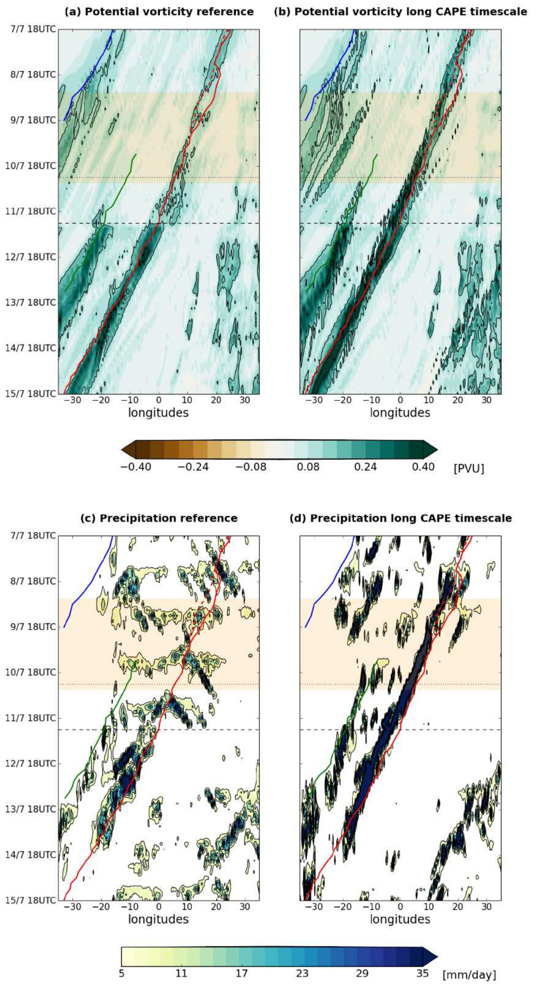

Figure 12. Hovmuller plots of potential vorticity (top row) and precipitation (bottom row) for the UM reference simulation (left column) and the UM long CAPE timescale sensitivity experiment (right column). The red solid line indicates the wave trough track as diagnosed from the analysis, the red dotted line as determined from the UM reference simulation. Only the forecast initial times July 7 00:00 UTC and July 11 00:00 UTC are used. The horizontal dotted line indicates the second forecast initialisation time, the horizontal dashed line indicates from which time on the data of the second forecast are used.

3.4. Potential vorticity analysis

In order to better understand the interaction between moist diabatic processes and the circulation a potential vorticity view is adopted. Recall that potential vorticity P is defined as

$$P = \frac{1}{\rho}\zeta^{\text{abs}} \cdot \nabla\theta \tag{3}$$

where ρ denotes density, ζ^{abs} absolute planetary vorticity, and θ potential temperature. Ertel's Theorem (Ertel 1942) states that

$$\frac{DP}{Dt} = \left(\frac{\zeta}{\rho}\right) \cdot \nabla S_\theta + \frac{\nabla\theta}{\rho} \cdot \nabla \times \mathbf{S_u} \tag{4}$$

Here S_θ and $\mathbf{S_u}$ represent sources of diabatic heating and friction, respectively. That is, the change of PV along an air trajectory is determined by the different diabatic source terms. On the mesoscale, PV can change due to convergence and divergence. The divergent part of the circulation may be a result of diabatic processes like convection (Hoerling 1992). It is therefore not possible to completely separate out impacts from adiabatic and diabatic processes on PV evolution. Nonetheless, equation (4) provides a useful framework for assessing the role of various diabatic sources of PV. Decomposing the diabatic source terms S_θ and $\mathbf{S_u}$ into a sum over different subgrid processes like convection, radiation, or boundary layer turbulent mixing, equation (4) can be written as

$$\frac{DP}{Dt} = \sum_{\substack{\text{parameterized}\\ \text{process } i}} \text{dPVtrac}_i \tag{5}$$

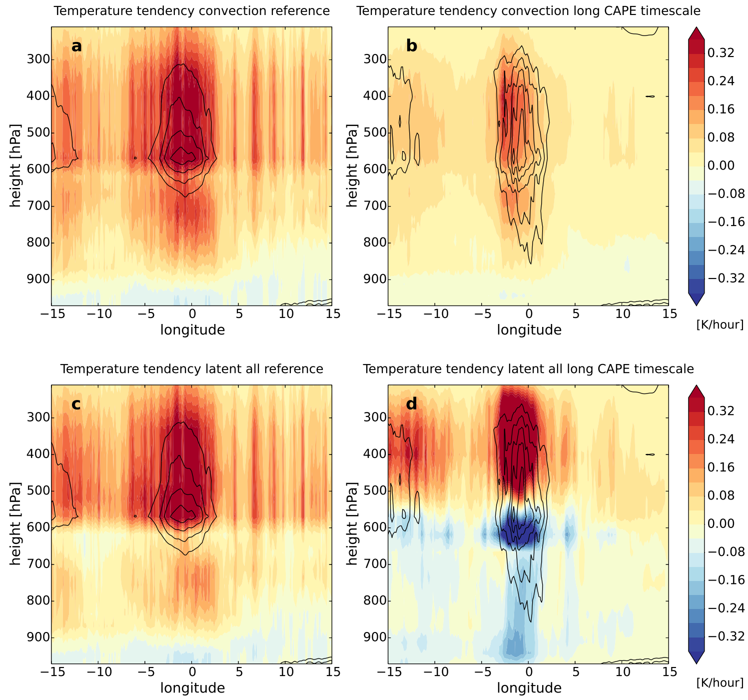

Figure 13. Mean longitude-height cross sections along the track for the temperature tendency from convection (top row), and the temperature tendency from convection plus large-scale precipitation (bottom row) for the UM reference simulation (left column) and the UM long CAPE timescale sensitivity experiment (right column). Black contours indicate corresponding mean PV along the track (contour lines are ±0.7, ±0.6, ±0.5, ±0.4, and ±0.3 PVU). Longitude 0 corresponds to the trough location of the wave.

Integrating both sides of the equation along a resolved flow trajectory $\vec{x}(t)$ of the model from time t_{start} to time t gives

$$\int_{t_{\text{start}}}^{t} \frac{DP}{Ds}\, ds = \sum_{\substack{\text{parameterized} \\ \text{process } i}} \text{PVtracer}_i(t) \qquad (6)$$

The individual terms PVtracer_i are called PV tracers, and were calculated along the model simulation in other contexts in previous studies (Gray 2006; Chagnon and Gray 2009; Chagnon *et al.* 2013). Thus, as implied by equation (6), the individual PV tracers are initialized with the value zero at the beginning of each forecast, and were calculated online during the model runs.

Figure 14 shows Hovmuller plots for PV tracers at 620 hPa for the convection parameterization and the large-scale precipitation scheme for the reference simulation (panels a and c) and the long CAPE timescale simulation (panels b and d), again using two forecast start times. In the reference simulation the convection parameterization does not generate high-PV air that ends up ahead of the trough. Rather, the PV generated by the convection parameterization tends to trail the trough (Figure 14, panel a). In the case of the long CAPE timescale simulation, high-PV air is created at and ahead of the trough by the large-scale precipitation scheme which contributes to intensifying the wave disturbance (Figure 14, panel d).

In principle convergence of PV could substantially contribute to the wave development. Panels e and f in Figure 14 show Hovmuller plots of the advection of the initial PV distribution by the resolved flow at 620 hPa, i.e. around the AEJ level. It shows that PV convergence does not substantially contribute to the intensification of the wave. If anything, PV tends to be transported away from the wave trough by the large-scale advection, especially in the long CAPE timescale simulation (Figure 14, panel f). Advection to a position ahead of the trough by the resolved flow might play a certain role in keeping the relative location of MCSs relative to the trough where they contribute to wave sustainment.

Thus latent heat release that occurs at and slightly ahead of the front is the main cause of the crucial strengthening of the dynamics of the wave. The results of Section 2 provided evidence that anomalous moisture convergence throughout the lower mid-troposphere initiate convection and updrafts in the region ahead of the trough. In Parker and Diop-Kane (2017, Section 3.1.4.1.4) it is suggested that the synoptic-scale vertical wind generated by

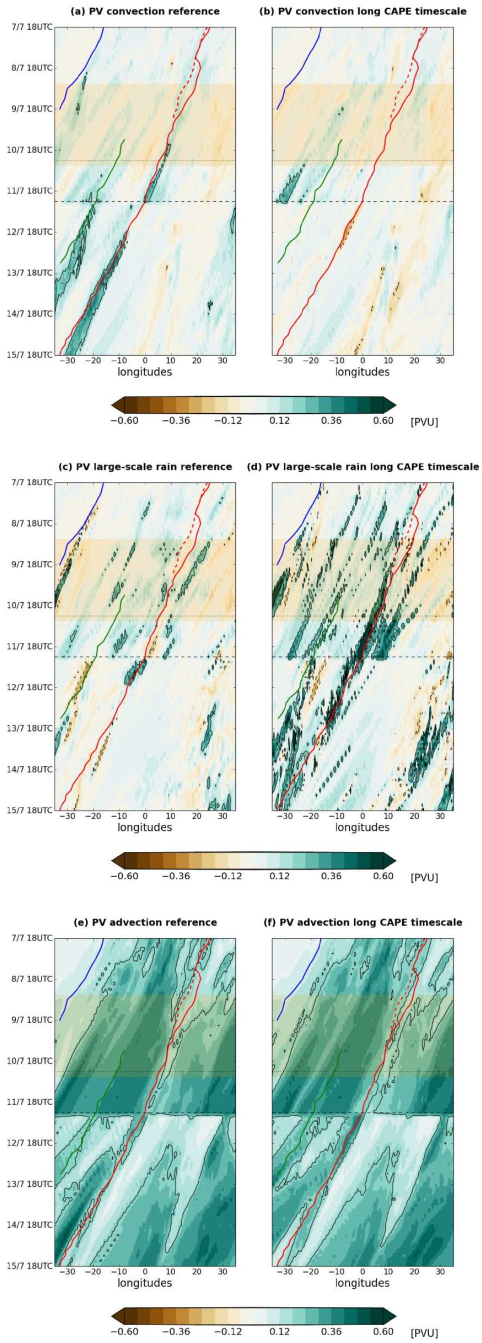

Figure 14. Hovmuller plots of the PV convection tracer (top row) and the PV microphysics tracer (middle row) at 620 hPa. The bottom row shows Hovmuller plots of the advected initial PV. Left column corresponds to the UM reference simulation (left column), right column to the UM long CAPE timescale sensitivity experiment. Only the forecast initial times July 7 00:00 UTC and July 11 00:00 UTC are used. The horizontal dotted line indicates the second forecast initialisation time, the horizontal dashed line indicates from which time on the data of the second forecast are used.

the waves are not strong enough to cause convective triggering. However, Wilson and Roberts (2006) reported that almost all MCSs considered in their study over the continental United States were initiated at convergence lines, either at lower or mid levels (see also Crook and Moncrieff (1988)). So what exactly induces convective activity at the crucial location at and slightly ahead of the trough?

In order to answer this question it is instructive to look at the horizontal structure of the interaction between latent heating and the anomalous wave circulation. Figure 15 shows the large-scale precipitation tracer in the long CAPE timescale simulation during the crucial strengthening phase of the wave. The clusters of high-PV air at and ahead of the trough associated with organized convection exhibit a scale that is much smaller than the scale of the wave disturbance. They are embedded in small regions of low-PV air. Only when the wave becomes more vigorous and the dynamics feeds back onto convection more strongly, the high-PV structures get more coherent and grow in scale (bottom panel in Figure 15).

This suggests that convection is initiated, and feeds back on the dynamics, in intense vortices on small scales.

This is confirmed when looking at a particular time in more detail, namely July 10 18:00 UTC. Panel a of Figure 16 shows the wind anomalies at 700 hPa in the long CAPE timescale simulation (colour shading indicates the meridional component of the wind), and panel b the precipitation. Organised convection is occurring just ahead of the trough. When examining cross sections 0.5 degrees longitude ahead of the trough, i.e. where precipitation develops, the instantaneous picture turns out to be consistent with the results of the composite analysis from Section 2. Below the level of the jet there is a cold anomaly (panel c), strongest moisture accumulation happens at lower mid-tropospheric levels of about 800 to 500 hPa. The moisture anomalies (panel d) correspond to regions of strongest vertical velocities (panel e), which are very localized. What is remarkable is that vertical velocities (colour shading in panel e) do not correspond to areas of horizontal convergence of the wind exactly (black contours in panel e). Rather, strongest horizontal convergence is observed at the edges of the mesoscale convective system, whereas the updrafts are located in its centre. Thus density effects are dominating the dynamics of the central region of organised convection. Panel f shows profiles of potential temperature and equivalent potential temperature at around the centre of the mesoscale convective system, between 12° to 13° North. The difficulty here is that profiles are partly a result of convective activity and have to be interpreted with care. Nevertheless, the equivalent potential temperature profile suggests that moist instability is found above the boundary layer in the lower mid-troposphere, and is mainly due to moisture effects. Thus local moisture convergence caused by the wave, and to some degree warm air advection from the north at mid-tropospheric levels, contribute to small-scale local organized convection and latent heat release which in turn reinforce the wave circulation.

That pockets of warm and stable air might play a role in wave sustainment is indicated by the PV tracers for boundary layer and radiative processes. Figure 17 shows PV tracers associated with the boundary layer and radiation parameterizations at a stage where the wave is fully developed and has reached the coastal region, i.e. on July 13 at 18:00 UTC. Behind the trough there is reduced influence from both processes due to the cold air advection. Throughout the wave development boundary layer mixing and radiation balance each other to a large degree. However, adding the two tracers reveals that there is structure in the sum of the two tracers that potentially plays a certain role for the wave dynamics.

Judging from the temporal development of the boundary layer tracer, the pocket of high-PV air at the wave trough at around 18° North is not solely due to advection from the north. The boundary layer parameterization contributes to the tracer during the day of July 13. The dynamics of the wave lifts the boundary layer top causing the boundary layer parameterization to mix deeper and more vigorously at and ahead of the trough where upward motion occurs. However, convection as well as precipitation happen more to the south between about 12 and 16 North. So to what degree the generation of high-PV air by northerly advection and dry mixing in the northern part of the disturbance is important for the wave dynamics needs further investigation.

Cross section plots of the four most important PV tracers show that only in the long CAPE timescale simulation does the contribution of latent heating at and slightly ahead of the trough contribute significantly to the wave dynamics (Figure 18). The PV contribution from the large-scale rainfall scheme occurs at the level of the AEJ or above. The integrated PV increments from the boundary layer parameterization and radiation occur mostly at lower levels. They largely balance each other and have their maxima further ahead of the trough, where warm air advection from the north is strongest. The potential role of boundary layer mixing ahead of the trough therefore requires further investigation.

4. African Easterly Waves as diabatic wave disturbances

The composite analysis based on objective AEW tracking presented in Section 2 together with the more detailed analysis of a strong wave in Section 3 allows for a conceptual picture of the interaction between moist diabatic processes and the atmospheric circulation in AEW propagation. Figure 19 shows two schematics which include the most important aspects. As discussed in Section 2 and pointed out in other studies (e.g., Janiga and Thorncroft 2016), the relative importance

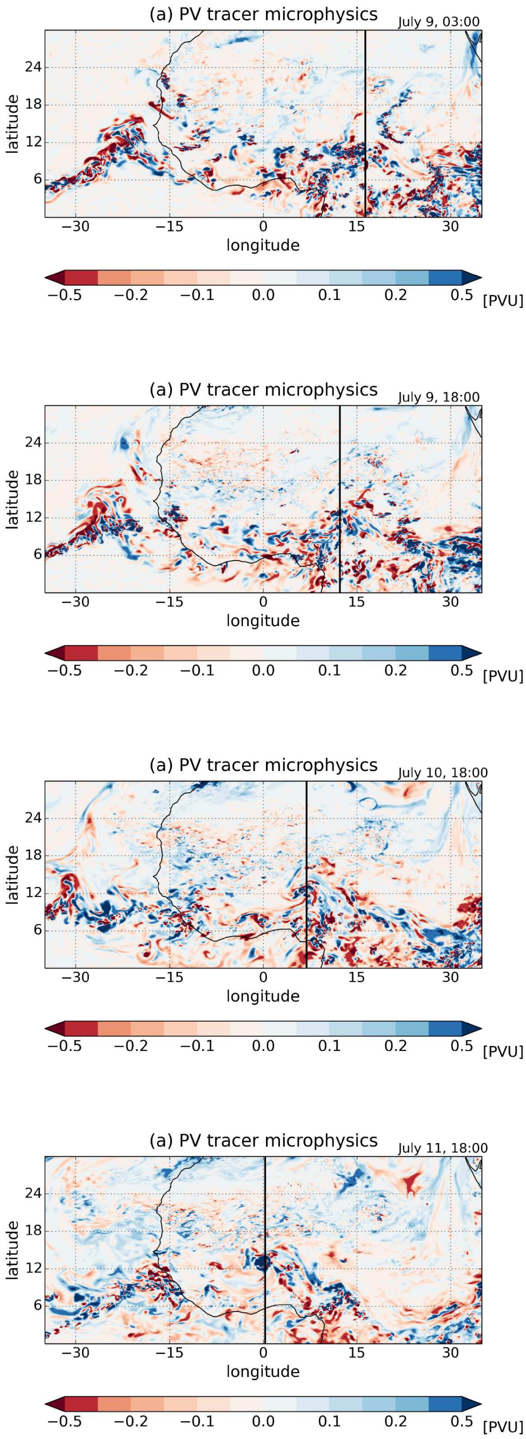

Figure 15. PV tracer for microphysics for the long CAPE timescale simulation during the strengthening phase of the wave at 700 hPa. The start time of the forecast is July 7 00:00 UTC.

of various features varies depending on the specific region and the corresponding climatological mean state. Also, the particular structure of AEWs can differ considerably from case to case (e.g., Berry and Thorncroft 2005; Bain *et al.* 2011; Ventrice and Thorncroft 2013), and in the AEW presented in Section 3 the relationship between moist convection and the wave dynamics is particularly strong. Typically the interaction between MCSs and AEWs is more loose and sporadic (Fink and Reiner 2003).

A starting point of a conceptual view on AEW propagation is the notion of a diabatic Rossby wave introduced in Parker and Thorpe (1995). Apart from barotropic aspects related to the instability of the AEJ, and possible extratropical influences, AEWs have a fundamental baroclinic structure due to the mean

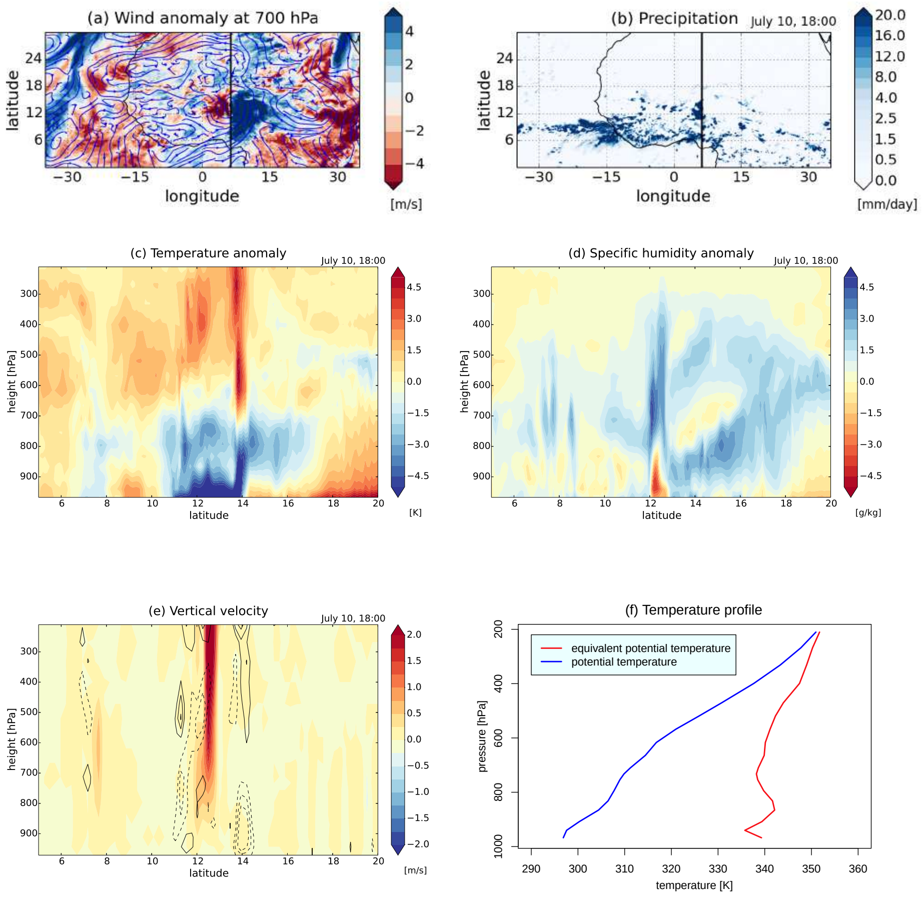

Figure 16. Wind anomalies (panel a) and precipitation (panel b) from the long CAPE timescale simulation for July 10, 18:00 UTC. The colour shading in panel a shows meridional wind. The trough location is indicated by a black vertical line. Panels c to e: Corresponding cross sections of temperature and specific humidity anomalies, and vertical velocity, respectively. The cross sections are located 0.5 degree longitude ahead of the trough where the organised precipitation is located. Anomalies are computed with respect to the mean over 9 days, and, in the case of the cross sections, the mean over $\pm 5^{\circ}$ longitudes around the trough location. The black contours in panel e indicate horizontal divergence of the wind (contour lines are ± 4.5, ± 3, and ± 1.5 $10^{-4}\mathrm{s}^{-1}$). Panel f: Temperature profiles 0.5 degree longitude ahead of the trough, averaged over latitudes 12 to 13, where the organised precipitation is located.

meridional temperature and humidity gradient in the region (Parker 2008). In the present paper it is demonstrated that diabatic moist processes at and slightly ahead of the trough intensify the dynamics of the wave. The main result of the study consists in showing that the wave circulation in turn organises convection preferentially at and slightly ahead of the trough through moisture convergence in the lower mid troposphere as sketched in panel a of Figure 19.

A three-dimensional view of the convection-circulation interaction in AEWs includes other aspects (panel b of Figure 19). Cooler and moister air is transported northward behind the trough, warmer and drier air is advected southward in front of the trough. As discussed in Section 2, there is a cross-frontal circulation which transports moisture to the area at and slightly ahead of the trough. The most important feature here is the lower to middle tropospheric moisture convergence at and slightly ahead of the trough which resembles a pre-frontal convergence line, and which triggers and feeds convective activity. The moisture convergence at and slightly ahead of the trough is combined with mid-tropospheric warm air advection from the north. These processes contribute to generating small-scale areas of large potential vorticity in which strong convective updrafts and latent heating occur. The latent heat release feeds back onto the circulation and intensifies the potential vorticity signature of the wave. The anomalous wave circulation in turn is conducive to advecting organised convection from the wave centre to locations slightly ahead of the trough, where it supports westward wave propagation. The interaction between moist convection and dynamics is thus fundamentally two-way in nature.

The present study hence highlights two important aspects. Firstly, the coupling of moist convection with the baroclinic dynamics of the waves occurs not within, but above the boundary layer, and mainly through moisture effects. Strongest moisture convergence occurs in the lower mid-troposphere,

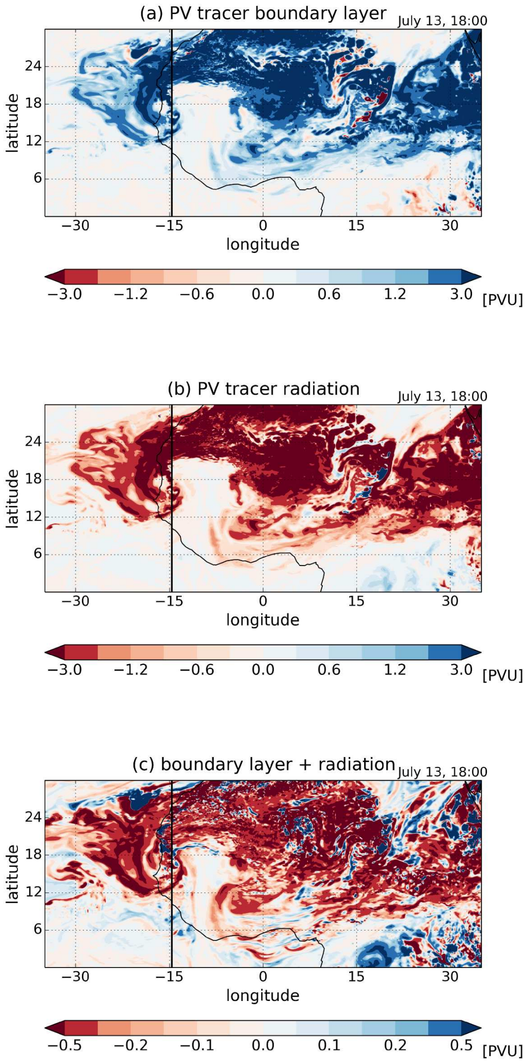

Figure 17. PV tracers for the boundary layer (panel a), the radiation (panel b), and the sum of the boundary layer and the radiation parameterizations (panel c) in the case of Jul 13, 18:00 UTC, at 700 hPa for the reference simulation. The forecast was initialised on July 11, 00:00 UTC.

roughly between 850 and 500 hPa. The wave is mainly cold core at around these heights, in contrast to the situation described in Parker and Thorpe (1995). At lower levels there are warm anomalies at and ahead of the trough only in the dry northern part of the domain. Furthermore, and this is the second important result of the present study, the cores of the MCSs which reinforce the wave through latent heating and corresponding upscale PV generation have a substantially smaller scale than the synoptic-scale baroclinic wave dynamics. Locally, however, the synoptic-scale wave may generate mesoscale convergence and moist instability which leads to convective activity ahead of the trough. Convection then feeds back onto the dynamics by latent heating and associated generation of strong PV anomalies, reinforcing the convective development and organization.

One might ask to what degree the crucial convection at and slightly ahead of the trough has to be considered forced convection in a conditionally unstable environment, or whether convection is generated mainly by moist static instability and buoyancy forcing. Clearly both aspects are intertwined, and the distinction is not clear-cut. Moisture and temperature advection by the synoptic-scale dynamics of the wave and related convergence can lead to local moist instability and vice versa. However, the evidence of the present study points at an important role of mid-tropospheric convergence lines or centres, i.e. mesoscale circulations which lead to moisture convergence, in initiating and organizing convection at and slightly ahead of the trough. Also Wilson and Roberts (2006) reported that almost all MCSs considered in their study over the continental United States were initiated at convergence lines, either at lower or mid levels.

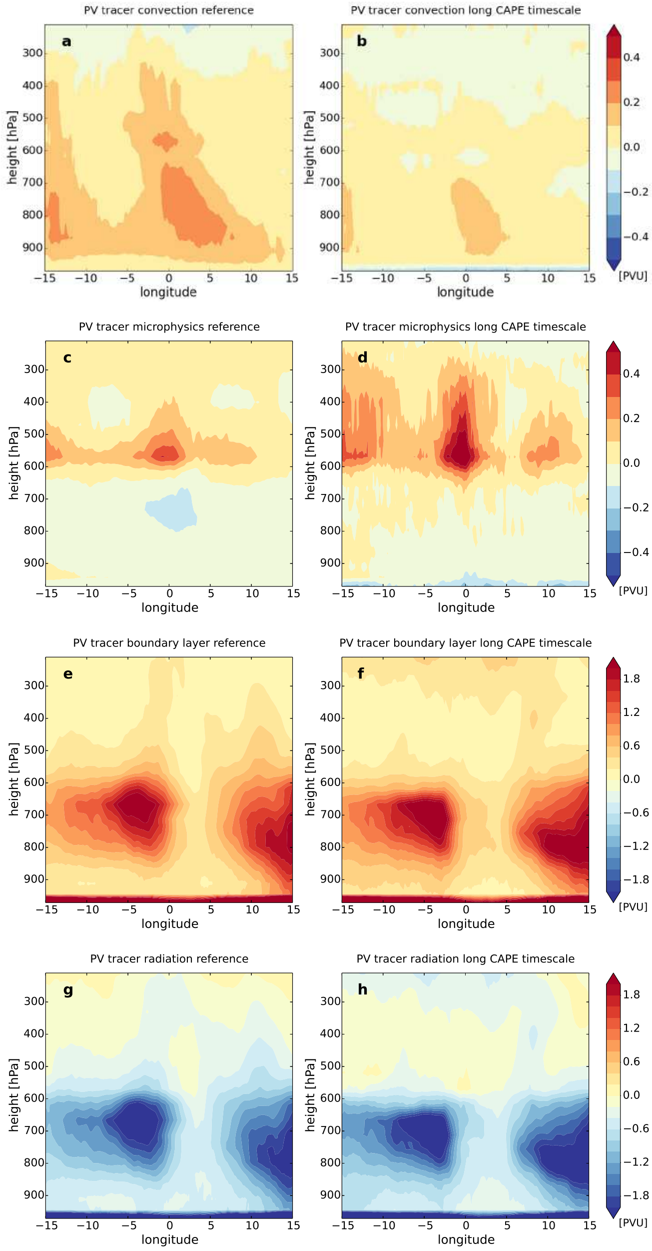

Figure 18. Mean longitude-height cross sections along the track for the PV convection tracer (first row), the PV microphysics tracer (second row), the PV boundary layer tracer (third row), and the PV radiation tracer (bottom row). Left column corresponds to the UM reference simulation, right column to the UM long CAPE timescale sensitivity experiment. Longitude 0 corresponds to the trough location of the wave.

And the case study presented in Bain *et al.* (2011) confirmed the important role of convergence, which lined the vorticity branches of the wave, for convective development. In the case investigated by Barthe *et al.* (2010) both CAPE and convective inhibition were poor predictors of MCSs ahead of the AEW trough, pointing at the important role of mesoscale circulations associated with the AEW in generating moist instability as well.

Advection of warm and stable air from the northern parts of the Sahel and the southern Sahara together with enhanced boundary layer mixing around the wave trough may result in small-scale structures of high-PV air at and ahead of the trough which potentially reinforce the PV signature of the wave disturbance. However, this potential mechanism of wave maintenance, indicated by our PV analysis, needs further investigation.

Most current convection parameterizations in numerical models are based on parcel theory and a diagnostic test parcel ascent, which neglects pressure gradients and considers only the buoyancy force. The parameterisations are designed to diagnose moist instability and remove it. Moreover, most deep convection parameterizations assume that convection is surface forced and rooted in the boundary layer. These assumptions lead to biases

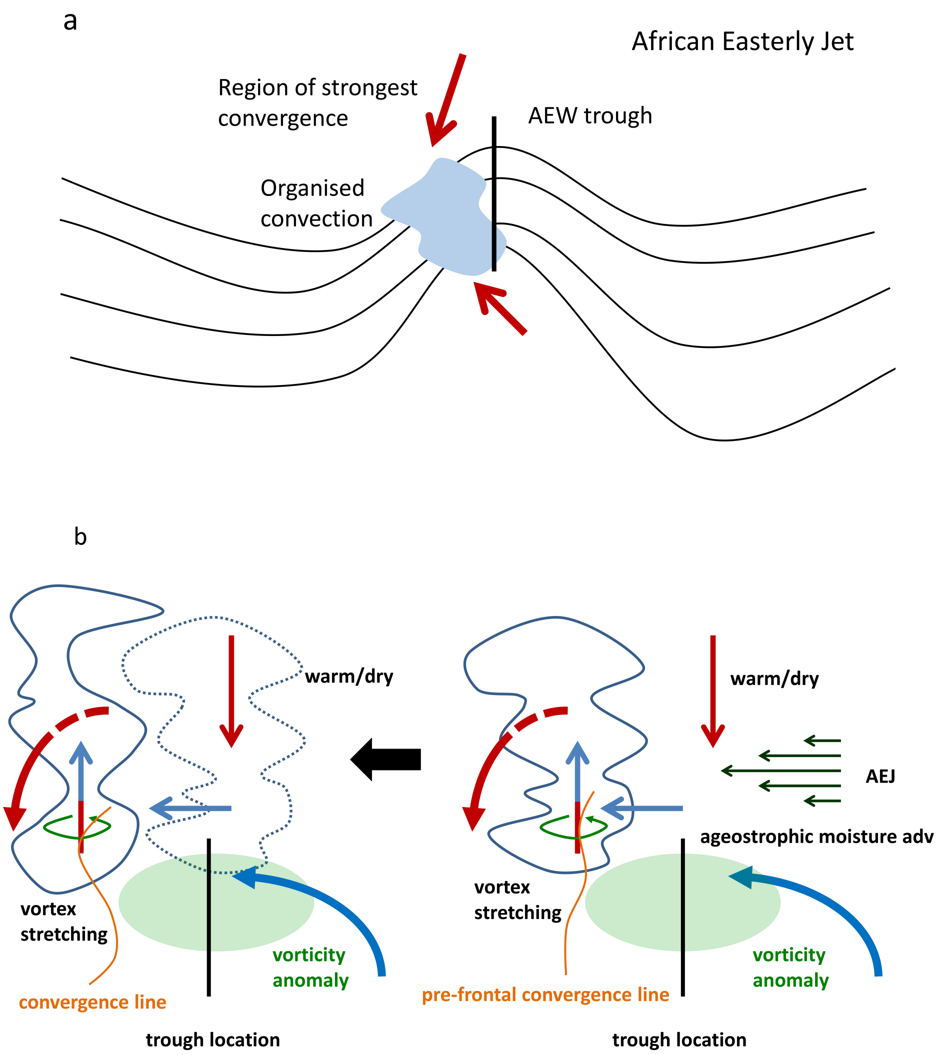

Figure 19. Panel a: horizontal perspective on the AEJ-AEW system: regions of strongest moisture convergence are located at and slightly ahead of the wave trough. This is the area where organised convection preferentially forms. Panel b: schematic of a three-dimensional view on the moist convection - dynamics interaction in African Easterly Wave propagation. Cool, moist air is advected northward behind the trough, warm and dry air is transported southward in front of the trough. A cross-frontal circulation provides the region at and slightly ahead of the trough with moisture. The lower mid-tropospheric moisture convergence at and slightly ahead of the trough triggers and organises convection. Strong updrafts in mesoscale convective systems slightly ahead of the trough generate potential vorticity through vortex stretching and support the wave propagation.

in the representation of tropical convection in many situations (Birch *et al.* 2014). Since according to our study convection is at least partly forced by local vorticity and convergence centres, this would explain why current convection parameterizations in numerical weather prediction and climate models struggle to correctly simulate the interaction between moist diabatic processes and the atmospheric circulation in AEWs. We plan to further investigate mesoscale circulations related to the interplay of AEWs and MCSs using high-resolution simulations in the future.

Acknowledgements

Helpful discussions with Martin Willett, Rachel Stratton, and David Walters are gratefully acknowledged. We thank Paul Earnshaw for technical assistance, Claudio Sanchez for support with the PV tracer diagnostics, and Romain Roehrig for advice regarding the calculation of Q_1^R. This work was supported by the Natural Environment Research Council/Department for International Development via the Future Climate for Africa (FCFA) funded project Improving Model Processes for African Climate (IMPALA, NE/M017265/1).

References

Bain CL, Parker DJ, Dixon N, Fink AH, Taylor CM, Brooks B, Milton SF. 2011. Anatomy of an observed African easterly wave in July 2006. *Q. J. R. Meteorol. Soc.* **137**: 923–933.

Bain CL, Williams KD, Milton SF, Heming JT. 2013. Objective tracking of African Easterly Waves in Met Office models. *Q. J. R. Meteorol. Soc.* **140**: 47–57.

Barthe C, Asencio N, Lafore JP, Chong M, Campistron B, Cazenave F. 2010. Multi-scale analysis of the 25-27 July 2006 convective period over Niamey: Comparison between Doppler radar observations and simulations. *Q. J. R. Meteorol. Soc.* **136**: 190–208.

Berry GJ, Thorncroft CD. 2005. Case study of an intense African Easterly Wave. *Mon. Wea. Rev.* **133**: 752–766.

Berry GJ, Thorncroft CD. 2012. African Easterly Wave dynamics in a mesoscale numerical model: the upscale role of convection. *J. Atmos. Sci.* **69**: 1267–1283.

Birch CE, Marsham JH, Parker DJ, Taylor CM. 2014. The scale dependence and structure of convergence fields preceding the initiation of deep convection. *Geophys. Res Lett.* **41**: 4769–4776.

Booth JF, Wang S, Polvani L. 2013. Midlatitude storms in a moister world: lessons from idealized baroclinic life cycle experiments. *Clim. Dyn.* **41**: 787–802, doi:10.1007/s00382-012-1472-3.

Burpee RW. 1972. The origin and structure of easterly waves in the lower troposphere of North Africa. *J. Atmos. Sci.* **29**: 77–90.

Chagnon JM, Gray SL. 2009. Horizontal potential vorticity dipoles on the convective storm scale. *Q. J. R. Meteorol. Soc.* **135**: 1392–1408.

Chagnon JM, Gray SL, Methven J. 2013. Diabatic processes modifying potential vorticity in a North Atlantic cyclone. *Q. J. R. Meteorol. Soc.* **139**: 1270–1282.

Charney JG. 1963. A note on the large-scale motions in the tropics. *J. Atmos. Sci.* **20**: 607–609.

Cornforth RJ, Hoskins BJ, Thorncroft CD. 2009. The impact of moist processes on the African Easterly Jet – African Easterly Wave system. *Q. J. R. Meteorol. Soc.* **135**: 894–913.

Craig G, Cho HR. 1988. Cumulus heating and CISK in the extratropical atmosphere. Part I: Polar lows and comma clouds. *J. Atmos. Sci.* **45**: 2622–2640.

Crook NA, Moncrieff MW. 1988. The effect of large-scale convergence on the initiation and maintenance of squall lines. *J. Atmos. Sci.* **45**: 3606–3624.

Dee DP, Uppala SM, Simmons AJ, Berrisford P, Poli P, Kobayashi S, Andrae U, Balmaseda MA, Balsamo G, Bauer P, Bechtold P, Beljaars ACM, van de Berg L, Bidlot J, Bormann N, Delsol C, Dragani R, Fuentes M, Geer AJ, Haimberger L, Healy SB, Hersbach H, Holm EV, Isaksen L, Kallberg P, Köhler M, Matricardi M, McNally AP, Monge-Sanz BM, Morcrette JJ, Park BK, Peubey C, de Rosnay P, Tavolato C, Thépaut JN, Vitart F. 2011. The ERA-Interim reanalysis: configuration and performance of the data assimilation system. *Q. J. R. Meteorol. Soc.* **137**: 553–597.

Ertel H. 1942. Ein neuer hydrodynamischer Wirbelsatz. *Meteor. Z.* **59**: 271–281.

Fink AH, Reiner A. 2003. Spatiotemporal variability of the relation between African Easterly Wave and West African Squall Lines in 1998 and 1999. *J. Geophys. Res.* **108**, doi:10.1029/2002JD002816.

Gray SL. 2006. Mechanisms of midlatitude cross-tropopause transport using a potential vorticity budget approach. *J. Geophys. Res.* **111**, doi:D17113.

Gregory D, Rowntree PR. 1990. A mass flux convection scheme with respresentation of cloud ensemble characteristics and stability-dependent closure. *Mon. Wea. Rev.* **118**: 1483–1506.

Guilloteau C, Roca R, Gosset M. 2016. A multiscale evaluation of the detection capabilities of high-resolution satellite precipitation products in West Africa. *J. Hydrometeor.* **17**: 2041–2059.

Hall NMJ, Kiladis GN, Thorncroft CD. 2006. Three-dimensional structure and dynamics of African Easterly Waves. Part II: Dynamical modes. *J. Atmos. Sci.* **63**: 2231–2245.

Hoerling MP. 1992. Diabatic sources of potential vorticity in the general circulation. *J. Atmos. Sci.* **49**: 2282–2292.

Hoskins BJ, Karoly DJ. 1981. The steady linear response of a spherical atmosphere to thermal and orographic forcing. *J. Atmos. Sci.* **38**: 1179–1196.

Hoskins BJ, Valdes PJ. 1990. On the existence of storm-tracks. *J. Atmos. Sci.* **47**: 1854–1864.

Houze RA. 1989. Observed structure of mesoscale convective systems and implications for large-scale heating. *Q. J. R. Meteorol. Soc.* **115**: 425–461.

Houze RA. 2004. Mesoscale convective systems. *Rev. Geophys.* **42**, doi: 10.1029/2004RG000150.

Hsieh JS, Cook KH. 2007. A study of the energetics of African Easterly Waves using a regional climate model. *J. Atmos. Sci.* **64**: 421–440.

Huffman GJ, Adler RF, Bolvin DT, Gu G, Nelkin EJ, Bowman KP, Hong Y, Stocker EF, Wolff DB. 2007. The TRMM multi-satellite precipitation analysis: Quasi-global, multi-year, combined-sensor precipitation estimates at fine scale. *J. Hydrometeor.* **8**: 38–55.

Janiga MA, Thorncroft CD. 2013. Regional differences in the kinematic and thermodynamic structure of African easterly waves. *Q. J. R. Meteorol. Soc.* **139**: 1598–1614.

Janiga MA, Thorncroft CD. 2014. Convection over tropical Africa and the East Atlantic during the West African Monsoon: regional and diurnal variability. *J. Climate* **27**: 4159–4188.

Janiga MA, Thorncroft CD. 2016. The influence of African Easterly Waves on convection over tropical Africa and the East Atlantic. *Mon. Wea. Rev.* **144**: 171–192.

Kiladis GN, Thorncroft CD, Hall NMJ. 2006. Three-dimensional structure and dynamics of African Easterly Waves. Part I: Observations. *J. Atmos. Sci.* **63**: 2212–2230.

Padro J. 1973. A spectral model for CISK-barotropic energy sources for tropical waves. *Q. J. R. Meteorol. Soc.* **99**: 468–479.

Parker DJ. 2008. A simple model of coupled synoptic waves in the land surface and atmosphere of the northern Sahel. *Q. J. R. Meteorol. Soc.* **134**: 2173–2184.

Parker DJ, Diop-Kane M (eds). 2017. *Meteorology of tropical West Africa: The forecaster's handbook*. Wiley-Blackwell: Oxford. 496pp.

Parker DJ, Thorpe AJ. 1995. Conditional convective heating in a baroclinic atmosphere: a model of convective frontogenesis. *J. Atmos. Sci.* **52**: 1699–1711.

Poan DE, Lafore JP, Roehrig R, Couvreux F. 2015. Internal processes within the African Easterly Wave system. *Q. J. R. Meteorol. Soc.* **141**: 1121–1136.

Reed RJ, Norquist DC, Recker EE. 1977. The structure and properties of African wave disturbances as observed during phase III of GATE. *Mon. Weath. Rev.* **105**: 317–333.

Roberts AJ, Marsham JH, Knippertz P. 2015. Disagreements in low-level moisture between (re)analyses over summertime West Africa. *Mon. Wea. Rev.* **143**: 1193–1211.

Skinner CB, Diffenbaugh NS. 2013. The contribution of African easterly waves to monsoon precipitation in the CMIP3 ensemble. *J. Geophys. Res. Atmos.* **118**: 3590–3609, doi:10.1002/jgrd.50363.

Thorncroft CD, , Hoskins BJ. 1994a. An idealized study of African Easterly Waves. I: A linear view. *Q. J. R. Meteorol. Soc.* **120**: 953–982.

Thorncroft CD, , Hoskins BJ. 1994b. An idealized study of African Easterly Waves. II: A nonlinear view. *Q. J. R. Meteorol. Soc.* **120**: 983–1015.

Ventrice MJ, Thorncroft CD. 2013. The role of convectively coupled atmospheric Kelvin waves on African Easterly Wave activity. *Mon. Wea. Rev.* **141**: 1910–1924.

Wilson JW, Roberts RD. 2006. Summary of convective storm initiation and evolution during IHOP: Observational and modeling perspective. *Mon. Weath. Rev.* **134**: 23–47.

Yanai M, Esbensen S, Chu JH. 1973. Determination of bulk properties of tropical cloud clusters from large-scale heat and moisture budgets. *J. Atmos. Sci.* **30**: 611–627.

